This paper has been published at P.H. Kuo, J. Du, Journal of American Ceramic Society 105 (2022) 3986-4008. doi.org/10.1111/jace.18391

Effect of boron oxide on mechanical and thermal properties of bioactive glass coatings for biomedical applications

Po Hsuen Kuo, Jincheng Du*

Department of Materials Science and Engineering, University of North Texas, Denton, TX 76203

(*Corresponding author. Email: du@unt.edu)

Abstract

Bioactive glass coatings can improve the osteo integration of metallic implants hence their lifespan and overall success rate. However, complex composition-structure-property relations in phosphosilicate-based bioactive glasses makes experimental determination of these relations and related composition design of bioactive coatings challenging. By applying molecular dynamics (MD) based atomistic simulations with recently developed effective potentials, this work addresses the challenge by using a material genome approach to obtain the composition and structure effect on various key properties for bioactive coating applications. A series of potential bioactive glass compositions were studied and the composition effect on the mechanical and thermal properties that are critical to these bioactive glasses as a coating to metallic implants were calculated. Particularly, by systematically varying the level of B₂O₃ to SiO₂ substitutions, the effect of composition on various key properties is elucidated. It was found that by using cation 1 to 1 ratio (BO_{3/2} to SiO₂) instead of the commonly used substitutions (B₂O₃ to SiO₂), the composition effect can be more clearly expressed and hence recommended in future composition designs. Importantly, together with careful structural analysis, the origin of property changes can be elucidated. The atomistic computer simulation-based approach is thus an effective way to guide future bioactive glass designs for bioactive coatings and other applications.

1. Introduction

Since its first discovery in 1970s, bioactive glass finds wide biomedical applications from hard tissue repair, wound healing, tissue engineering, to bioactive coatings to metallic implants [1-6]. Metallic implants such titanium and alloys are widely used in load bearing orthopedic operations and joint replacements. To date, almost one million arthroplasties were performed annually, and the number is expected to reach 3.5 million by 2030 [7–9]. Despite high success rate of orthopedic implantation surgery, there are increasing cases of deterioration, tissue intoxication, and prolong postoperative recovery, commonly caused by the interfacial instability, mechanical loosening, accidental infection, and foreign body reaction elicited by the implants [3,10–13]. After the implanting surgery, a non-adherent and fibrous granulation tissue often encapsulates the implant as a spontaneous response to foreign objects from the host [14–17]. To better integrate the metallic implant with the host tissue, hence improve the overall longevity of the implants, coating metal with a layer of bioactive material has been extensively studied. The only FDA-approved process is coating the metal implants with hydroxyl apatite, the mineral part of bone, through thermal spray. Another promising way extensively explored in the past two decades is to coat the metal implants with bioactive glasses, an inorganic material can form bonds with soft or hard tissues [18–24]. The first bioactive glasses invented by Larry Hench in early 1970s is based on the SiO₂-Na₂O-CaO-P₂O₅ system while later studies have expanded the glass composition ranges significantly [25–27]. It is now accepted that the dissolution of alkali ions in the glass when in contact with body fluid leads to the formation of hydrated and porous amorphous silica layer where calcium and phosphate groups are absorbed. The absorbed amorphous calcium phosphate can crystallize the hydroxyapatite (HAp, Ca₁₀(PO₄)₆(OH)₂, Ca-apatite) on the surface [28–30], providing a compatible environment for osteoblast cell proliferation in the host body. It was also found that, together with HAp, the local liquid ionic environment can promote bone cell growth, providing an adhesive, strong biological interfacial bond between the bioactive glass layer and the host tissue, enhancing biocompatibility of the implants [31–36]. As a coating material, the dense glass structure can also seal the substrate, preventing the corrosion and release of heavy metal ions [24,37-40].

Among the properties of bioactive glasses as coatings to metallic implants, the matching of the coefficient of thermal expansion (CTE) with the substrate metal is an important consideration. A large mismatch of CTE can lead to thermal stresses or even cracks at the glassmetal interface hence weaken the interfacial bonding during the coating process [11,41]. The

viscous sintering method have been used widely to coat various bioactive glasses on metal implant surfaces [13,42–45]. It was found that there is a trade-off needs to be made between the homogeneity of coating glass and the chemical stability of the interface [46,47]. Recently, laser-assisted coating used to apply bioactive glass coatings on metal implants, high laser energy melts bioactive glass and metal to form cladding layer and prompt a strong interfacial bonding [19,48,49]. However, the high energy density also induces tensile stress and elemental dilution between the glass and heat affect zone of metal, which change the chemical composition and microstructure of the glass and can decrease the biological response [49–51]. It is thus clear that designing bioactive glass coating for metal implants is a challenging task due to large design space of potential glass compositions, various targeted thermal, mechanical and bioactivity properties, and available coating methods.

The physical and biological properties of bioactive glasses can be adjusted by changing the glass compositions. Indeed, bioactivity, the dissolution rate, mechanical properties, and thermal properties can be modified by doping or substituting major oxides in the base bioactive glass composition [52-61]. B₂O₃ has been proven to accelerate both glass degradation and HAp crystallization [62–68]. Some research also shows that substituting SiO₂ of bioactive glasses with B₂O₃ (B₂O₃/SiO₂) or adjusting the ratio of B₂O₃/SiO₂ in bioactive glass can enhance the density of HAp on the glass surface without causing static local environment that inhibits cell proliferation [32,62,63,69,70]. For thermal properties, it was found that adding B₂O₃ in CaO-SiO₂-P₂O₅ bioactive glass can lower the sintering temperature during coating and increase the homogeneity of glass layer [71]. Xie et al. reported that doping 4% of B₂O₃ enhances the density and mechanical properties of 45S5 Bioglass® coating without sacrificing the bioactivity[72]. Although the optimal composition is not yet reached, the targets of bioactive glass coating can be summarized from the previous investigations: (1) The CTE of bioactive glass should be close to but slightly higher than that of metal implant to create a compressive stress on the interface to increase the adhesion [73,74]. (2) T_g of bioactive glass needs be lower than the sintering temperature to allow viscous sintering to form a uniform glass layer on the surface of metal implant with complex shape [75]. (3) The mechanical properties of bioactive glass should be sufficiently high after coating process to prevent interfacial crack or delamination from the micromovement or strain [7,31,76]. (4) The bioactivity of glass needs to be preserved after coating without the elemental dilution or crystallization of the coating layer during the coating process.

With more complexity and functionality involved in bioactive glasses, the conventional "cook-and-look" methods gradually become infeasible and resource-consuming endeavor. Owing to the unique amorphous structure, a glass does not need to satisfy the stoichiometric requirement as crystalline material. This high compositional continuity allows glass to incorporate with nearly every element on periodic table, creating an essentially infinite number of compositions. Following the concept of "material genome", the "glass genome" concept has been proposed to take advantage of the vast composition space to design glass for various applications [77,78]. Both physics-based and numerical based modeling approaches can be used in "glass genome" to design glasses for various technological and biomedical applications [77,79,80]. To raise a few examples, artificial neural network (ANN) was adapted to develop models to predict T_g, tensile strength [81– 83], molecular dynamic (MD) simulation was adapted to large-scale sequential compositional exploration and structural analysis [84,85], and topological model was developed to predict the initial dissolution rate of glass [86,87]. For the current work, a combination of physics modeling such as MD simulations based on recent developed partial charge effective potentials and Quantitative Structure-Property Relationship (QSPR) analysis were adopted to help elucidate the major contributor of glass properties and leading the direction to functional-oriented compositional optimization [84,85,88–92].

MD simulations have showed that with increasing level of SrO/CaO substitution causes a weaker Si-O network, and lower shift of PQn and SiQn species in 4585 Bioglass® [1, 94]. The change in medium-range structure creates an open network for Na⁺ diffusion thus provide the evidence that agrees with the experimental result of the positive effect on the bioactivity. With the development of rigid ion [106] or polarizable potentials [118] for boron oxide, the effect of boron oxide to silica substitution on the structures of phosphosilicate based bioactive glasses have been investigated [95, 117]. Integrating MD simulations and solid-state NMR have revealed significant short and medium range structure details of these glasses as a result of boron oxide to silica substitution [117]. The preference of NBO association with glass former oxygen structural units were established, as well as the probability of glass former cation-oxygen-glass former linkages [117]. MD simulation found that B₂O₃/SiO₂ substitution in Sr-doped 55S4.3 Hench Bioglass® shows an abrupt decrease in bioactivity when the network connectivity (NC) increases from 2.6 in 0%-B₂O₃/SiO₂ to over 3 in 25%-B₂O₃/SiO₂. The value 2.6 of NC was considered as the upper boundary in compositional modification [95], which can be the increase of additional amount of

glass former resulted from the substitution SiO₂ with B₂O₃ in 1:1 molar ratio. Although most of experimental study was done by molar ratio substitution, the increase of B can lead to the increase of NC and thus hinder the biological response. However, at the same time, the local environment of boron has always been a complicated field and affects the final glass properties largely.

This paper reports an investigation of designing bioactive glass compositions, particularly by boron oxide to silica substitutions, suitable for bioactive coatings of metal implants by using atomistic simulations and related property calculations. Bioactive glass 6P55 (composition: 54.5SiO₂-11.6Na₂O-2.6K₂O-16.1CaO-12.7MgO-2.5P₂O₅, in mol %) was used as the matrix due to its high glass stability and its CTE (11.1x10⁻⁶/K) is close to titanium alloy (Ti6Al4V, 9.5-10.5x10⁻⁶/K) [41,96]. As compared to other bioactive glasses, e.g. 45S5, these glasses have higher stability against crystallization, due to introducing K₂O and MgO oxides in the glass composition, hence is more suitable for sintering. By optimizing the firing conditions, bioactive coatings with higher interfacial strength have been applied to titanium and cobalt-chromium alloys by using the viscous sintering method [41]. The focus of this work is to study the effect of boron oxide to silica substitution on the structures and various physical properties of 6P55 bioactive glasses. Although not found in the original Hench bioactive glass compositions, boron oxide has been shown to improve hot forming domain [97], provide beneficial effect on bioactivity [32,68,98,99], increase corrosion resistance (e.g. in Pyrex[©] glass) [100], and can potentially improve the adhesion with the metal implants [95,101]. It is thus of significant importance to study the effect of boron oxide addition to bioactive glasses for bioactive coating applications. In mixed former glasses, there are two schemes of substitution: one is based on general chemical formula B₂O₃ to SiO₂ substitution while the other one is BO_{3/2} to SiO₂ based substitution. The latter is based on cation 1 to 1 ratio substitution. The two would lead to difference in composition and hence the glass properties. In order to compare the effect of the two types of substitutions two series of glasses have been studied. The first series consists of 5%, 10% and 15% of B₂O₃/SiO₂ substituted 6P55, which is the conventional way of boron oxide to silica substitution, while the second series consists of 5%, 10% and 15% of BO_{3/2}/SiO₂ substituted 6P55 to keep total glass former cation constant in the substituted glasses. Detailed structural analyses were performed for the two series of bioactive glasses. The structural changes are correlated with their mechanical, thermal properties as a function of glass composition and the structural origins of these changes are elucidated.

2. Methodologies

2.1 Glass formation using MD simulations

The selected bioactive glass composition for coating were studied using classical MD simulations with Large-scale Atomics/Molecular Massively Parallel Simulator (LAMMPS) program[102]. Table 1 shows the compositions and densities of the glasses investigated in this study. The 6P55 bioactive glass was chosen as the base glass and glasses with 0, 5, 10 and 15 mol% B₂O₃ to SiO₂ substitution were studied and denoted as 6P55 x%B₂O₃ (where x = 5, 10, 15). The B/Si ratio of each glass composition and percentages of non-bridging oxygen (NBO) from the final simulated glasses are also shown in Table 1. The B/Si ratio increases more rapidly in the 1:2-sub series than the 1:1-sub series, not surprisingly. While the NBO percentage decreases in the 1:2-sub series, it increases monotonically in the 1:1-sub series. The compositions correspond to the conventional ways of conducting B₂O₃/SiO₂ experiment [103,104]. We also investigated 6P55 with 5, 10, 15 mol% BO_{3/2} to SiO₂ substitution were denoted as 6P55 $x\%BO_{3/2}/SiO_2$ (where x = 5, 10, 15). The compositions were designed by the atomistic view of glass structure, using BO_{3/2}/SiO₂ substitution to keep the amount of glass former constant. We focused on the compositions with less or equal to 15 mol% B₂O₃ or BO_{1.5} to SiO₂ substitution as higher level of substitutions decrease the thermal, chemical stability [95] and overall bioactivities [120, 121] of the glasses that make them not suitable for bioactive coating applications. Each simulation cell contains around 10,000 atoms and three parallel simulations were carried out for each composition. Glass series with B₂O₃/SiO₂ substitution are labeled as "1:2-gf-sub" and those with BO_{3/2}/SiO₂ substitution are labeled as "1:1-gf-sub".

The partial charge pairwise potential with short-range interaction in the Buckingham form and long-range Coulombic interaction was set to describe the interatomic energy, as shown in Eq 1.

$$V(r_{ij}) = \frac{q_i q_j e^2}{4\pi \varepsilon_0 r_{ij}} + A_{ij} \exp\left(\frac{-r_{ij}}{\rho_{ij}}\right) - \frac{c_{ij}}{r_{ij}^6} \qquad --(1)$$

where V and r_{ij} are the potential energy and interatomic distance between ion i and j, respectively. The first term describes the long-range Coulombic interaction. q_i and q_j are the partial atomic charge of ion i and j and ε_0 is the electrical permittivity in vacuum. The second and third terms

describe the exponent of the Buckingham form repulsive energy and van dar Walls attraction energy. The potential parameters in second and third terms of Equation 1, A_{ij} , ρ_{ij} and C_{ij} , were developed by Deng and Du, as shown in Table 2 [105]. The initial simulation cell was created by a random atomic configuration equilibrated at 298K for 20 ps using isothermal-isobaric (NPT) ensemble for the structural relaxation. The simulation cell was then melted at 3500K using NPT ensemble for 200 ps, before quenched from 3500K to 300K at a cooling rate of 5K/ps using NPT ensemble. The final equilibrium steps were carried out at 300K using NPT, canonical (NVT) and then microcanonical (NVE) ensembles for 100 ps, respectively. The final glass was extracted from the last trajectory of NVE equilibrium. Fig. 1 shows the snapshot of the structure bioactive glass 6P55_10%B₂O₃ and the zoomed in picture showing the network structure consisting of SiO₄, BO₃, BO₄ and PO₄ units.

2.2 Calculation of coefficient of thermal expansion

The coefficient of thermal expansion (CTE) of glass was measured by recording the volume of simulation cell from 298K to 2298K in 100K intervals. The glass was kept at each temperature for 50ps using NPT ensemble at 1 atm to reach equilibrium. A volume-to-temperature diagram was firstly established to determine the glass transition temperature (Tg). Then, the CTE was derived from Eq 2 using the temperature below Tg of each composition specifically.

$$\alpha_L = \frac{1}{\partial T} \frac{\partial L}{L_0} \qquad --(2)$$

where α_L represents the linearly coefficient of thermal expansion, L_0 represents the original length of the simulation box and ∂L represents the length change corresponds to the temperature change ∂T .

2.3 Calculation of mechanical properties

The mechanical property is calculated from the micro-deformation process performed in MD simulation, which is defined as the strain caused by the stress, as expressed by the Eq 3.

$$\sigma_i = C_{ij} \times \varepsilon_j \qquad \qquad --(3)$$

where σ_i is the symmetric stress tensors elements, ε_j is the responding symmetric strain elements, and C_{ij} (i, and j are the Voigt deformation component. i and j = 1, 2, 3, 4, 5, 6) is the elastic constant

tensor. A finite deformation of 0.5% was applied from six directions (x, y, z, xy, yz, xz) of simulation cell using method by Aidan Thompson to obtain the elastic constant matrix (C) [108], after that, the compliance matrix (S) can be derived from the inverse of elastic constant matrix ($S = C^{-1}$). Voigt, Reuss and Hill's methods were adopted to calculate Bulk (S) and shear modulus (S). Voigt method uses uniform strain in the aggregation, and the equation for Voigt bulk and shear modulus were shown in Eq 4 and 5.

$$B_{Voigt} = \frac{1}{9} (C_{11} + C_{22} + C_{33} + 2(C_{12} + C_{13} + C_{23})) \quad -(4)$$

$$G_{Voigt} = \frac{1}{15} (C_{11} + C_{22} + C_{33} - (C_{12} + C_{13} + C_{14}) + 3(C_{44} + C_{55} + C_{66})) \quad -(5)$$

On the other hand, Reuss method uses the uniform stress in the aggregation to acquire bulk and shear modulus, as shown in Eq 6 and 7.

$$B_{Reuss} = (S_{11} + S_{22} + S_{33} + 2(S_{31} + S_{21} + S_{32}))^{-1} - (6)$$

$$G_{Reuss} = \frac{15}{4(S_{11} + S_{22} + S_{33} - S_{12} - S_{23} - S_{13}) + 3(S_{44} + S_{55} + S_{66})} - (7)$$

The Young's modulus of both methods can be calculated by Eq. 8.

$$E = \left(\frac{1}{3G} + \frac{1}{9B}\right)^{-1} - (8)$$

For statistical accuracy, Young's modulus of bioactive glass reported in this paper were calculated from Hill's method, which is the geometric average of Voigt and Reuss methods [109].

3. Results

3.1 The effect of B₂O₃ substitution on the short-range structure of major glass former

The structural information of simulated bioactive glass 6P55, 6P55 with B₂O₃/SiO₂ substitution series and 6P55 with BO_{3/2}/SiO₂ substitution series were captured by coordination number (CN), total correlation function (TDF), pair distribution function (PDF) and Q_n species.

Fig 2 shows the results of TDF and CN of Si-O and P-O in 6P55. The bond distances of Si-O and P-O are 1.60 Å and 1.51 Å, respectively, and both Si and P are in the four-fold oxygen coordinated environment. Three parallel tests show the same result, suggesting that both

tetrahedral SiO₄ and PO₄ are stable in 6P55 bioactive glass. Fig 3 shows the TDF and CN of Si-O, B-O and P-O of 1:2-gf-sub. Fig 3-(a) and (c) shows that the SiO₄ and PO₄ tetrahedrons are still stable in the glass with increasing B₂O₃/SiO₂. The TDF and CN of Si-O and P-O can be found in Fig 4-(a) and (c), which are as same as Fig 2 of 6P55, and Fig 3-(a), (c) of 1:2-gf-sub series. The result suggests that the short-range structure of Si and P are not affected by the compositional change.

On the other hand, different ratio of glass former substitution results diverse change in the local environment of boron. Fig. 3-(b) and 4-(b) shows that the B-O distance decreases as the amount of B₂O₃ increases and SiO₂ decreases in the glass. The plateau of B-O CN drops from 3.5 to 3.1 as B₂O₃/SiO₂ increases in 1:2-gf-sub series and the plateau of B-O CN drops from 3.7 to 3.1 as BO_{3/2}/SiO₂ increases in 1:1-gf-sub. The result indicates a mix of three-fold-oxygen coordinated boron (B^[3]) and of 4-fold-oxygen coordinated boron (B^[4]) exist in glass, and the amount of B^[3] increases and the amount of B^[4] decrease with increasing B₂O₃/SiO₂.

Therefore, the short-range environment of $B^{[3]}$ and $B^{[4]}$ were shown by deconvoluting PDF of $B^{[3]}$ -O and $B^{[4]}$ -O . For 1:2-gf-sub, Fig. 5 shows that the bond distance of $B^{[3]}$ -O decreases from 1.42 Å to 1.39 Å with B_2O_3/SiO_2 increases from 5% to 10% and stop changing with B_2O_3/SiO_2 increases from 10% to 15%; the intensity of PDF peak has no obvious change as B_2O_3/SiO_2 increases. For 1:1-gf-sub, Fig. 6 shows that both peak positions and intensity change continuously. Bond distance of $B^{[3]}$ -O decrease from 1.45 Å to 1.41 Å to 1.38 Å and the bond distance of $B^{[4]}$ -O decrease from 1.53 Å to 1.51 Å to 1.45 Å as $BO_{3/2}/SiO_2$ increase from 5% to 10% to 15%. The change of B-O bond distance and the percentage of $B^{[3]}$ and $B^{[4]}$ in the glass was summarized in Table 3 and 4, respectively.

3.2 The effect of boron oxide substitution on the medium range structure of major glass formers

Bond angle distribution (BAD) between major glass formers were calculated to depict the connection between polyhedrons. As a general observation, Fig 7 and 8 show an expanding angle of \angle Si-O-B < \angle Si-O-Si < \angle Si-O-P in both series of glasses, which should be resulted from the increasing columbic repulsive force between Si⁴⁺ \leftrightarrow B³⁺, Si⁴⁺ \leftrightarrow Si⁴⁺ and Si⁴⁺ \leftrightarrow P⁵⁺. For the BAD of

Si-O-Si, Fig 7-(a) shows ∠Si-O-Si of 1:2-gf-sub is a constant of 150° with increasing B₂O₃/SiO₂. On the other hand, Fig 8-(a) shows that ∠Si-O-Si of 1:1-gf-sub decreases from 151° to 147° series with increasing BO_{3/2}/SiO₂. For the BAD of Si-O-B, Fig 7-(b) shows ∠Si-O-B increases from 143° to 150° as B₂O₃/SiO₂ increase from 5% to 10%. On the other hand, Fig 8-(b) shows ∠Si-O-B expand continuously from 142° to 149° with increasing BO_{3/2}/SiO₂. For the BAD of Si-O-P, ∠Si-O-P in 1:2-gf-sub (Fig 7-(c))is around 3° wider than ∠Si-O-P in 1:1-gf-sub series (Fig 8-(c)). However, no clear results can be interpreted from BAD of B-O-P because of the low intensity.

To investigate in the compositional effect, the deconvolution of \angle Si-O-B^[3] and \angle Si-O-B^[4] are calculated and presented in Fig 9 and 10. General observation shows that both \angle Si-O-B^[3] and \angle Si-O-B^[4] expand in both 1:1-gf-sub and 1:2-gf-sub glasses. Comparing between Fig 9-(a) and (b), the intensity of \angle Si-O-B^[3] increases and the intensity of \angle Si-O-B^[4] decreases as B₂O₃/SiO₂ increases. Furthermore, \angle Si-O-B^[3] does not expand and stay at a constant 148.5° for all B₂O₃/SiO₂, while the \angle Si-O-B^[4] expands from 140.5° to 148.5° as B₂O₃/SiO₂ increases from 5% to 10%. A different behavior can be found in 1:1-gf-sub. As shown in Fig. 10-(a) and (b), \angle Si-O-B^[3] expands continuously from 145° to 150°, and \angle Si-O-B^[4] also expands from 141° to 150°, as BO_{3/2}/SiO₂ increases. Although substituting B₂O₃ with SiO₂ should increases the network connectivity due to the increase of glass former, it is not the only factor. The expansion between SiO₄-BO₄ contributes majorly to the structural change in 1:2-gf-sub; while the expansion of SiO₄-BO₄ and SiO₄-BO₃ both contribute to the structural in 1:1-gf-sub glass. Since the connection between major polyhedrons respond differently to the B₂O₃ substitution, these two methods could not only result to different structural properties but also thermal and mechanical properties.

3.3 The effect of B₂O₃ substitution on the Q_n species of glass formers

The distribution of Q_n species represents the strength of network structure thus is highly related to the mechanical, chemical properties and bioactivity of the glass. Q_n species here represents a glass former cation-oxygen tetrahedron with n bridging oxygen. For boron, as it can take 3 and 4-fold coordination of oxygen, the boron species is denoted as $B_n^{[m]}$, in which m represents boron coordination and n presents the number of bridging oxygen, or B_n , where n is the average number of bridging oxygen and calculated based on the fraction of $B^{[3]}$ and $B^{[4]}$ species.

The distributions of the three major glass formers species for the 1:2-gf-sub and 1:1-gf-sub series were calculated and presented in Fig 11, 12, and 13.

For SiQ_n species, Fig 11-(a) shows SiQ₁ and SiQ₂ decrease while SiQ₃ and SiQ₄ increases with increasing B₂O₃/SiO₂ in 1:2-gf-sub series glasses. Fig. 11-(b) shows that the change of SiQ_n species of 1:1-gf-sub is not significantly affected by compositional change from the 6P55, suggesting that keeping same glass former ratio does not drastic alter the network connection, thus, could have lower effect on the dissolution behavior.

For PQn species, Fig. 12-(a) shows PQ0 and PQ1 decrease and PQ2 and PQ3 increase, indicating an increasing number of P-BO (P- bridging oxygen) with increasing B2O3/SiO2 in 1:2-gf-sub series. Fig. 12-(b) show that PQ1, PQ2 and PQ3 decrease as PQ0 increases, suggesting an increase in P-NBO (non-bridging oxygen) with increasing BO3/2/SiO2 in 1:1-gf-sub. MD simulation shows that the connection of PO4 tetrahedron in glass network decreases in 1:1-gf-sub, but increases in 1:2-gf-sub with increasing B2O3. The increase of higher *n* PQn species in the 1:2 substitution series can be explained by the double amount of former cations introduced for each substitution hence there are more bridging oxygen and the network becomes more connected. For 1:1 substitution series, each B can form maximum 3 or 4 bridging oxygens, depending on its coordination, hence the total bridging decreases that resulting in a decrease of higher *n* PQn species and increase of PQ0 species. ³¹P NMR studies showed that P ions in glasses exist mainly as Q0 and small amount of Q1 species [119]. MD simulations tend to overestimate the higher n Qn species of P and the results are dependent on the choice of interatomic potential [95, 117]. It has been shown that the usage of polarizable potentials in MD simulations can improve the description phosphorus Qn distribution than the rigid ion potential used in this work [117-119].

For boron species, Fig. 13-(a) and (b) show both substitution series lead to an increase of B_0 , B_1 and B_2 percentages and a decrease of B_3 and B_4 percentages with increasing the level of substitution. However, it can be seen that the change of B_n has a more consistent change in the 1:1-gf-sub series (Fig. 13 b) than the 1:2-gf-sub series. All B_4 species come from 4-fold coordinated boron while B_3 can from 4 or 3-fold coordinated boron. The $B_n^{[3]}$ (n=0-3) and $B_n^{[4]}$ (n=0-4) distributions of 3- and 4-fold coordinated boron for two glasses are shown in Fig. S1. The majority species are $B_4^{[4]}$ and $B_3^{[4]}$ for 4-fold coordinated boron and $B_2^{[3]}$, $B_3^{[3]}$ and $B_1^{[3]}$ species for 3-fold coordinated boron. It is worth mentioning that there are small amount $B_0^{[3]}$ species (ranging

from 1.8 to 4.4% depending on the composition) but no $B_0^{[4]}$ species was observed. The percentages of boron spices $B_n^{[4]}$ and $B_n^{[3]}$ as a function of the B/Si ratio for the two series of glasses are summarized in Fig. S2. The change can be explained by the amount of bridging oxygen in the system as a function of the substitution discussed earlier. Table 5 summarizes the change of Si and P Q_n , as well as B_n , species as a function of substitution concentration and Fig. 14 shows representative configurations of different Q_n species in the glasses.

3.4 Tg and CTE of B₂O₃ substituted 6P55 bioactive glass

 T_g of all compositions were acquired by step heating method and the CTE of each composition is calculated from the volume change below the T_g . Fig 15-(a) shows the fitting of T_g of 6P55 bioactive glass as a demonstration: two tangent lines ($R^2 \ge 0.97$) were fitted and extended from the lower and higher temperature regions to find the intersection as T_g . In Fig 15-(b), both 1:2-gf-sub and 1:1-gf-sub show the same pattern of decreasing T_g with increasing B₂O₃ substitution. Unlike 1:1-gf-sub series, the decreasing pattern of 1:2-gf-sub discontinues when B₂O₃/SiO₂ concentration increase above 10%. Overall, the T_g value of all 1:2-gf-sub glass are higher than 6P55. On the contrary, T_g of all 1:1-gf-sub glasses are all lower than 6P55.

Figure 16 (a) shows the CTE fitting of 6P55 with 10% BO_{3/2}/SiO₂ substitution and Figure 16 (b) summarized the CTEs of all the glasses. The CTE of 1:2-gf-sub glasses decreases from 1.82×10⁻⁵ K⁻¹ to 1.76×10⁻⁵ K⁻¹ and remain constant when the composition reaches 10% B₂O₃/SiO₂ substitution. For 1:1-gf-sub series, the CTE continuously decreases from 1.76×10⁻⁵ K⁻¹ to 1.75×10⁻⁵ K⁻¹ then to 1.73×10⁻⁵ K⁻¹ as BO_{3/2}/SiO₂ increases hence shows a more linear change with the level of substitution. The evolution of thermal properties can be correlated to structural changes that are summarized in Table 5, particularly those of B^[3] and B^[4] concentrations and associated Q_n species change. The more linear change of CTE in the 1:1 substitution series makes composition design more easily to achieve than the 1:2 substitution series.

3.5 Mechanical Properties: Bulk, Shear and Young's Modulus

The mechanical property primarily determines the longevity, rate of revision surgery and risk of toxicity release of biomedical implant. Bulk, shear and Young's moduli of calculated from MD simulations are shown in Fig. 17. In Fig 17-(a) and (b), the bulk modulus increases while the shear modulus decreases with increasing BO_{3/2}/SiO₂. On the other hand, the bulk modulus of 1:2-gf-sub differs little from that of 6P55 and shows little change with increasing B₂O₃/SiO₂. The shear modulus of 1:2-gf-sub, shows an increase at 5% B₂O₃/SiO₂ but gradually decreases with increasing B₂O₃/SiO₂. Young's modulus of both 1:1-gf-sub and 1:2-gf-sub decreases with increasing substitution, and the Young's modulus of 1:1-gf-sub are found to have higher value than 1:2-gf-sub.

4. Discussion

4.1 Influence of B₂O₃ substitution to the thermal properties of 6P55

Thermal properties such as T_g and CTE of bioactive glass 6P55 with B₂O₃/SiO₂ (1:2-gf-sub) and BO_{3/2}/SiO₂ (1:1-gf-sub) substitution were calculated from MD simulations. We have shown that the structural features of these two series of B₂O₃ substitutions are quite different and, therefore, the following section will discuss how the change of thermal properties with composition are correlated with glass structure changes.

In the previous section, Fig 18-(b) shows that 1:2-gf-sub series have higher T_g than the original 6P55 glass, the value decreases with increasing B_2O_3/SiO_2 and reaches a plateau at 10% to 15% concentration. On the other hand, the T_g of 1:1-gf-sub series continuously decreases with increasing $BO_{3/2}/SiO_2$ substitution. To explain the difference, the change of network connectivity (NC) as a function of increasing substitution concentration was calculated by Eq. 8 and shown in Fig 18-(a). NC increases linearly from 2.5 (6P55 bioactive glass) to ~2.68 in 1:2-gf-sub series, but linearly decreases to ~2.32 in 1:1-gf-sub series. The increasing trend of NC in the 1:2-gf-sub series is mainly due to the additional glass former cation (boron) introduced to the composition, which is also reflected from the higher intensity and higher angle of \angle Si-O-B BAD peak. The NC is defined as:

$$NC = \frac{\sum_{n=0}^{4} \{n \cdot Si_{n} \cdot N_{Si} + n \cdot B_{n}^{[3]} \cdot N_{B[3]} + n \cdot B_{n}^{[4]} \cdot N_{B[4]} + n \cdot P_{n} \cdot N_{P}\}}{N_{Si} + N_{B[3]} + N_{B[4]} + N_{P}} - (9)$$

where Si_n and P_n represents percentage of Si and P Qn species, respectively; $B_n^{[3]}$ and $B_n^{[4]}$ represent percentages of 3- or 4-fold coordinated boron with n bridging oxygen, respectively; N_{Si} , N_P , $N_{B^{[3]}}$ and $N_{B^{[4]}}$ represent the number of Si, P, B^[3] and B^[4] cations in the formula or the simulation cell.

A linear increase of NC in the 1:2 gf-sub series does not lead to a linear change in T_g. Fig 18-(a) shows T_g of 1:2-gf-sub decreases from 1450K to 1426K when B₂O₃/SiO₂ increases from 5% to 10% and does not change as B₂O₃/SiO₂ increases from 10% to 15%. On the other hand, the T_g of 1:1-gf-sub decrease almost linearly as a function of BO_{3/2}/SiO₂ substitution. Comparing the change of boron coordination number and B_n from 1:2-gf-sub and 1:1-gf-sub, Table 5 indicates that, in 1:2-gf-sub glass, 37% of B^[4] converts to B^[3] when B₂O₃/SiO₂ increase from 5% to 10%, and only 1% variation between 10% and 15% B₂O₃/SiO₂. Moreover, Si/B ratio of 15% B₂O₃/SiO₂ in 1:2-gf-sub is 1.3, the value implies that B₂O₃/SiO₂ substitution makes B replacing Si as the major network former with additional boron doping. The result suggests that the contribution of NC is not the predominant factor of the thermal properties. In fact, the change of local structure of the glass formers should have higher influence.

For 1:1-gf-sub, the decreasing trend of T_g coincides with the decreasing NC, which is reasonable because of substituting $Si^{[4]}$ with increasing $B^{[4]}$ and some $B^{[3]}$. Since there is no additional glass former, the network energy can be used to determine the thermal property. As $BO_{3/2}/SiO_2$ increases, $B^{[3]}$ and $B^{[4]}$ should have increasing influence on the glass structure. Besides the coordination number, probing into the conversion of B_n species can help us understand the change of local environment of glass former. From the research by Mauro et al. using binary glass system, $xM_2O-(1-x)B_2O_3$ (M= glass modifier), the increases of x within the range of $0 \le x \le \frac{1}{3}$ results to B_3 converting to B_4 , which increase the T_g . Further increases x in $x > \frac{1}{3}$ regime leads to lower distribution of B_n species [110]. Fig 18-(c) shows that the decreasing trend of T_g of 1:1-gf-sub and 1:2-gf-sub can be contributed by the lower shifting in B_n , corresponding to the fact that lower B_n species of B (B_1 , and B_2) is contributed by $B^{[3]}$, and higher B_n species is contributed by $B^{[4]}$.

In 1:2-gf-sub, the B₁ and B₂ converting to B₃ and B₄, and the conversion trend slightly deflect at B₂O₃/SiO₂, which corresponds to the T_g shown in Fig 15-(b). In 1:1-gf-sub (black), B₃ and B₄ converting to B₂ and even B₁. However, we must consider the change of SiQ_n species because of the additional glass formers. As shown in Fig 18-(d). 1:2-gf-sub shows a relatively steady amount of SiQ₃, while 15% of SiQ₂ converting to SiQ₄ with increasing B₂O₃/SiO₂, which reduce the T_g. In 1:2-gf-sub 15% glass, since SiQ₄ is higher than the original 6P55, the T_g value of 1:2-gf-sub is higher than the 6P55. For 1:1-gf-sub glasses, SiQ₂ linearly increase to 32.5% in 15% BO_{3/2}/SiO₂, both SiQ₃ and SiQ₄, slightly increase at 5% BO_{3/2}/SiO₂ then decrease to a lower value compared to 6P55.

From MD simulation, we can deduct that the local structure of B_n and SiQ_n can better describe the compositional effect on T_g of 6P55 bioactive glass. And the additional boron in B_2O_3/SiO_2 substitution results to higher NC, which makes NC inaccurate when estimating the thermal property.

4.2 The influence of boron local environment to CTE

CTE depends on the amplitude of thermal vibration in the glass network, therefore , the stronger bonding within network constrains the vibration amplitude, which should reduce CTE and increases T_g . Since CTE is considered as a dynamic expansion of endothermic reaction, with the constant heat flow (∂T in Eq. 2) in MD simulation, the structural change as a function of temperature should play the essential role for the CTE. Fig 16-(b) shows both series have decreasing CTE with increasing B_2O_3 , and 1:1-gf-sub series have more continuous trend of CTE change than 1:2-gf-sub. Therefore, a reasonable deduction can be made that the change of $B^{[3]}$ and $B^{[4]}$ as a function of temperature should also determine the sensitivity of the structural response to thermal energy. The variation between $B^{[3]}$ and $B^{[4]}$ in 1:1-gf-sub and 1:2-gf-sub at increasing temperature were shown in Fig 19-(a) and (b), respectively.

Fig 19 shows that $B^{[4]}$ gradually converts to $B^{[3]}$ as temperature increases, and this structural change should be reversible as the cell temperature decrease within the temperature range below T_g . Moreover, the $B^{[4]} \rightarrow B^{[3]}$ has a saturation point where $B^{[4]}$ and $B^{[3]}$ can only reach 90% and 10% at high temperature to keep the glass structure stable. Fig. 19-(a) shows that ~44% and ~22%

of $B^{[4]}$ converting to $B^{[3]}$ in 5% and 10% $BO_{3/2}/SiO_2$ as temperature increase from 498K to 2298K, respectively. In Fig 19-(b), 1:2-gf-sub shows little change of $B^{[3]}$ and $B^{[4]}$, except in 5% B_2O_3/SiO_2 , where ~30% of $B^{[4]}$ converts to $B^{[3]}$ as temperature increases. Since the BAD shows $\angle Si-O-B^{[3]}$ is higher than or equal to $\angle Si-O-B^{[4]}$ in all compositions (Fig 9 and 10), it can be deducted that the cell expansion could be contributed by the expanding angle between SiO_4 and BO_3 units. The cell expansion responding to increasing temperature will be held back when no more BO_3 unit is created and all BO_4 is stabilized, thus explain the trend of CTE.

This $B^{[4]} \rightarrow B^{[3]}$ conversion also affects the distribution of B_n species during temperature increase. Since the BO₃ majorly contribute to the increasing amount of B₂, the increase of B₂ is an indication of $B^{[4]} \rightarrow B^{[3]}$ conversion after absorbing the thermal energy [105]. Fig. 20-(a) shows the B_n change during heating, B_4 is converting to B_2 , while B_0 , B_1 and B_3 shows a little change from the 498K to T_g , suggesting the thermal energy is used to converting $B^{[4]}$ into $B^{[3]}$, and thus the glass network weaken as cell expand. The similar behavior can be found in Fig 20-(b) and (d). However, in Fig. 20-(c), 15% $BO_{3/2}/SiO_2$ shows a $B_4 \rightarrow B_3$ while B_2 remains almost constant. In this composition, the CTE stops decreasing because no further increase in $B^{[3]}$. The same composition with "saturated $B^{[3]}$ " can be found in Fig. 20-(e) and (f) for 10% and 15% of B_2O_3/SiO_2 , respectively. This evidence explains the limitation of modifying composition to adjust thermal for 6P55 using B_2O_3/SiO_2 substitution.

Overall, the comparison of thermal properties suggests that 1:1-gf-sub allows more control over the glass structure and their thermal properties than the conventional 1:2-gf-sub 6P55, which induced excessive B₂O₃ that changes 6P55 into boron-dominated glass. The 1:2-gf-sub 6P55 should be considered as B₂O₃-doped 1:1-gf-sub 6P55.

4.3 Comparison of CTE from empirical models

CTE has been a hidden issue when designing the bioactive glass compositions, there are many studies pointing out some glasses have high bioactivity have to be sacrificed for the coating procedure due to the large difference of CTE between glass and metal [12,49,76]. Another approach is to predict the CTE by the weight ratio of oxides and their proportionality factors. D. Bellucci et

al. and S. Lopez-Esteban et al. summarized the factors of currently available models using a general additive equation, as shown in Eq. 10 [41,73].

$$CTE = \sum_{i}^{n} \alpha_{i} p_{i} - (10)$$

where α_i is the proportionality factor and p_i is the wt. % of oxides; and n is the total number of the oxide in glass. The α_i of corresponding oxides used this study are listed in Table 6. It is important to note that the $\alpha_{P_2O_5}$ shown in Winkelmann & Schott's model was from mathematic derivation, which does not include in other empirical models. Because of the essentiality of P_2O_5 in bioactive glass, $\alpha_{P_2O_5}$ was added from the study of Hench et al to all models and is denoted as P_2O_5 [111].

The CTE resulted from the aforementioned models were shown in Fig 21-(a) and (b) for 1:2-gf-sub and 1:1-gf-sub, respectively. For 1:2-gf-sub series (Fig. 21(a)), all the models predict a decrease of CTE with increasing the level of substitution, but the Hall model predicts the least change of CTE in the series which may be caused by the fact that $\alpha_{B_2O_3}$ is larger than α_{SiO_2} in Hall's model. On the other hand, most models predict the CTE increases with increasing BO_{3/2}/SiO₂ substitution in the 1:1-gf-sub series. One exception is the E.T. model, which predicts a slight decrease of CTE with increasing the level of substitution. The prediction of the E.T. model is in agreement with those from MD simulations (see Fig. 16(b)). This confirms the predictive capacity of the E.T. model, which is supported by several previous studies [73,115,116].

4.4 The effect of B₂O₃ substitution to the mechanical properties of 6P55

The bulk modulus represents how resistance of glass to compression stress and the shear modulus represents the stiffness of the glass to the shear stress, as shown in Eq 11 and 12.

$$K = -V \frac{dP}{dV} = \rho \frac{dP}{d\rho} - (11)$$

where K represents the bulk modulus, dP is the change of compression force and dV is the change of volume as a response to dP. With constant mass, the bulk modulus, K, also equals to the change of density, ρ , as response to compressive stress. To put it simply, the less the change of glass structure, the larger the K value.

$$G = \frac{\tau_{xy}}{\gamma_{xy}} = \frac{F}{Atan\theta} - (12)$$

where G represents the shear modulus, τ_{xy} represents the shear stress, which is equal to the ratio of shear force (F) exerted on an area(A), and θ represents the shear angle of the structure. To find the correlation between structural properties and mechanical properties, plots of NC vs bulk, shear and Young's modulus were shown in Fig 22. In Fig 22-(a), it is interesting to find that with increasing NC, the bulk modulus of 1:2-gf-sub do not change significantly with increasing B2O3/SiO2, and the bulk modulus of 1:1-gf-sub only changes slightly from 28GPa to 29GPa with increasing BO3/2/SiO2. This can be explained by the stronger SiO4 connection in 1:1-gf-sub with compositional change. As shown in Fig 11, the B2O3 substitution causes an increase in the SiQn in 1:2-gf-sub while 1:1-gf-sub remain almost unchanged. However, the stronger connection around SiO4 does not enhance the mechanical properties, suggesting that other glass former has large influence on the mechanical properties when using 1:2-gf-sub. Fig. 22-(b) shows that the shear modulus of 1:1-gf-sub decreases as NC decreases, which is fairly reasonable. On the other hand, 1:2-gf-sub decreases as NC increase. This behavior is similarly to T_g shown in Fig. 15-(b), implying that B_n species could have major influence the shear modulus of of bioactive glass.

5. Conclusions

In this paper, the capability of using MD based atomistic simulations and associated property calculations to design the composition of bioactive glasses for biomedical applications, with a particular focus on bioactive coatings for metal implants, has been investigated. The CTE, Tg, bulk, shear and Young's modulus of bioactive glass 6P55, which is a bioactive glass composition with high thermal stability and matching CTE with titanium alloy, together with two series of compositions with B₂O₃/SiO₂ and BO_{3/2}/SiO₂ substitutions, have been systematically studied using MD simulations with recently developed effective partial charge potentials to understand how boron oxide to silica substitution affect the physical properties of these glasses.

Short and medium range structures such as boron coordination, glass former cation Q_n distribution and network connectivity of the glasses were obtained and correlated with the property changes with composition. The results show that the network connectivity is a general indicator of change of T_g : Si Q_n and B_n distribution change shows the conversion of $B_4 + B_3 \rightarrow B_2 + B_1$ and Si

 $[Q_4 + Q_3 \rightarrow Q_2]$ can decrease the T_g. Furthermore, B₂O₃ to SiO₂ substitution was found to increase T_g, due to an increase of network connectivity. It is known that boron coordination change with composition is both a function of R (modifier to boron ratio) and K (silicon to boron ratio) and shows a nonlinear dependence of R and K. In the composition range studied (B₂O₃ or BO_{3/2} < 15 mol%), using BO_{3/2} to SiO₂ substitution gives more linear and monotonic changes of T_g, CTE and other properties than the conventional B₂O₃ to SiO₂ substitution hence is recommended for composition design.

The changes of properties of bioactive glasses with composition and their structural origins, were also investigated. To understand the CTE of these glasses, boron local environment as a function of temperature was extracted from simulations. It was found that the conversion of $B^{[3]} \rightarrow B^{[4]}$, which results in a larger angle between Si-O-B (\angle Si-O-B^[4] > \angle Si-O-B^[3]), is the major contribution to thermal expansion with temperature. For B₂O₃ to SiO₂ substitution, the CTE shows a saturation effect with the level of substitution. For glasses with BO_{3/2} to SiO₂ substitution, it shows a more linear change with composition in the substitution level studied (up to 15 mol%). The CTE from MD simulation is further compared with several existing models of CTE and the effectiveness of the models were compared and discussed. Mechanical properties in terms of shear, bulk and Young's moduli in the two kinds of substitutions were also investigated. For B₂O₃ to SiO₂ substitution leads to a decrease of shear and Young's modulus, which is mainly due to the decrease of Si Q_n species. On the other hand, BO_{3/2} to SiO₂ substitution does not have large effect on the mechanical properties. The results show that MD based simulation is an effective approach to design bioactive glass compositions for coating and other biomedical applications.

Acknowledgements

We gratefully acknowledge support of the U.S. National Science Foundation (Project #1662288). The authors acknowledge the Talon 3 system at The University of North Texas for providing High Performance Computing resources that have contributed to the research results reported within this paper.

References

- [1] M. Montazerian, E. Dutra Zanotto, History and trends of bioactive glass-ceramics, Journal of Biomedical Materials Research Part A. 104 (2016) 1231–1249. https://doi.org/10.1002/jbm.a.35639.
- [2] J.R. Jones, D.S. Brauer, L. Hupa, D.C. Greenspan, Bioglass and Bioactive Glasses and Their Impact on Healthcare, International Journal of Applied Glass Science. 7 (2016) 423–434. https://doi.org/10.1111/ijag.12252.
- [3] E. Lenguerrand, M.R. Whitehouse, A.D. Beswick, S.K. Kunutsor, P. Foguet, M. Porter, A.W. Blom, Risk factors associated with revision for prosthetic joint infection following knee replacement: an observational cohort study from England and Wales, The Lancet Infectious Diseases. 19 (2019) 589–600. https://doi.org/10.1016/S1473-3099(18)30755-2.
- [4] L.J. Hawke, N. Shields, M.M. Dowsey, P.F.M. Choong, N.F. Taylor, Effectiveness of behavioural interventions on physical activity levels after hip or knee joint replacement: a systematic review, Disability and Rehabilitation. 0 (2019) 1-. https://doi.org/10.1080/09638288.2019.1603328.
- [5] G. Hooper, The ageing population and the increrasing demand for joint replacement, The New Zealand Medical Journal. 126 (2013) 2–3. https://doi.org/10.2106/JBJS.F.00222.Annual.
- [6] M. Fang, N. Noiseux, E. Linson, P. Cram, The Effect of Advancing Age on Total Joint Replacement Outcomes, Geriatric Orthopaedic Surgery & Rehabilitation. 6 (2015) 173–179. https://doi.org/10.1177/2151458515583515.
- [7] L. Gaviria, J.P. Salcido, T. Guda, J.L. Ong, Current trends in dental implants, Journal of the Korean Association of Oral and Maxillofacial Surgeons. 40 (2014) 50. https://doi.org/10.5125/jkaoms.2014.40.2.50.
- [8] C.D. Etkin, B.D. Springer, The American Joint Replacement Registry—the first 5 years, Arthroplasty Today. 3 (2017) 67–69. https://doi.org/10.1016/j.artd.2017.02.002.
- [9] A.M. Halder, T. Gehrke, C. Günster, K.D. Heller, H. Leicht, J. Malzahn, F.U. Niethard, P. Schräder, J. Zacher, E. Jeschke, Low Hospital Volume Increases Re-Revision Rate Following Aseptic Revision Total Knee Arthroplasty: An Analysis of 23,644 Cases, Journal of Arthroplasty. 35 (2020) 1054–1059. https://doi.org/10.1016/j.arth.2019.11.045.
- [10] K.J. Bozic, S.M. Kurtz, E. Lau, K. Ong, D.T.P. Vail, D.J. Berry, The epidemiology of revision total hip arthroplasty in the united states, Journal of Bone and Joint Surgery Series A. 91 (2009) 128–133. https://doi.org/10.2106/JBJS.H.00155.
- [11] J. anne N. Oliver, Y. Su, X. Lu, P.H. Kuo, J. Du, D. Zhu, Bioactive glass coatings on metallic implants for biomedical applications, Bioactive Materials. 4 (2019) 261–270. https://doi.org/10.1016/j.bioactmat.2019.09.002.
- [12] A. Kirsten, A. Hausmann, M. Weber, J. Fischer, H. Fischer, Bioactive and thermally compatible glass coating on zirconia dental implants, Journal of Dental Research. 94 (2015) 297–303. https://doi.org/10.1177/0022034514559250.
- [13] S. Omar, F. Repp, P.M. Desimone, R. Weinkamer, W. Wagermaier, S. Ceré, J. Ballarre, Sol–gel hybrid coatings with strontium-doped 45S5 glass particles for enhancing the performance of stainless steel implants: Electrochemical, bioactive and in vivo response, Journal of Non-

- Crystalline Solids. 425 (2015) 1–10. https://doi.org/http://dx.doi.org/10.1016/j.jnoncrysol.2015.05.024.
- [14] J.M. Anderson, A. Rodriguez, D.T. Chang, Foreign body reaction to biomaterials, Seminars in Immunology. 20 (2008) 86–100. https://doi.org/10.1016/j.smim.2007.11.004.
- [15] R. Trindade, T. Albrektsson, P. Tengvall, A. Wennerberg, Foreign Body Reaction to Biomaterials: On Mechanisms for Buildup and Breakdown of Osseointegration, Clinical Implant Dentistry and Related Research. 18 (2016) 192–203. https://doi.org/10.1111/cid.12274.
- [16] D.C. Hansen, Metal corrosion in the human body: The ultimate bio-corrosion scenario, Electrochemical Society Interface. 17 (2008) 31–34.
- [17] J. Black, Does corrosion matter?, Journal of Bone and Joint Surgery Series B. 70 (1988) 517–520. https://doi.org/10.1302/0301-620x.70b4.3403590.
- [18] S.R. Paital, N.B. Dahotre, Calcium phosphate coatings for bio-implant applications: Materials, performance factors, and methodologies, Materials Science and Engineering R: Reports. 66 (2009) 1–70. https://doi.org/10.1016/j.mser.2009.05.001.
- [19] S.R. Paital, N.B. Dahotre, Wettability and kinetics of hydroxyapatite precipitation on a laser-textured Ca-P bioceramic coating, Acta Biomaterialia. 5 (2009) 2763–2772. https://doi.org/10.1016/j.actbio.2009.03.004.
- [20] G. Graziani, M. Bianchi, E. Sassoni, A. Russo, M. Marcacci, Ion-substituted calcium phosphate coatings deposited by plasma-assisted techniques: A review, Materials Science and Engineering C. 74 (2017) 219–229. https://doi.org/10.1016/j.msec.2016.12.018.
- [21] T.S. Technology, R.C. Tucker, Introduction to Coating Design and Processing, Thermal Spray Technology. 5 (2018) 76–88. https://doi.org/10.31399/asm.hb.v05a.a0005725.
- [22] L.L. Hench, O. Andersson, M. McLaren, D.E. Niesz, Bioactive Glass Coatings, An Introduction to Bioceramics. 23 (1993).
- [23] J.M. Gomez-Vega, E. Saiz, A.P. Tomsia, T. Oku, K. Suganuma, G.W. Marshall, S.J. Marshall, Novel Bioactive Functionally Graded Coatings on Ti6Al4V, Advanced Materials. 12 (2000) 894–898. https://doi.org/10.1002/1521-4095(200006)12:12<894::AID-ADMA894>3.0.CO;2-4.
- [24] S. Hiromoto, M. Tomozawa, Hydroxyapatite coating of AZ31 magnesium alloy by a solution treatment and its corrosion behavior in NaCl solution, Surface and Coatings Technology. 205 (2011) 4711–4719. https://doi.org/10.1016/j.surfcoat.2011.04.036.
- [25] L.L. Hench, Bioceramics: From Concept to Clinic, Journal of the American Ceramic Society. 74 (1991) 1487–1510. https://doi.org/10.1111/j.1151-2916.1991.tb07132.x.
- [26] W. Cao, L.L. Hench, Bioactive materials, Ceramics International. 22 (1996) 493–507. https://doi.org/10.1016/0272-8842(95)00126-3.
- [27] J.R. Jones, L.M. Ehrenfried, L.L. Hench, Optimising bioactive glass scaffolds for bone tissue engineering, Biomaterials. 27 (2006) 964–973. https://doi.org/10.1016/j.biomaterials.2005.07.017.

- [28] G. Kaur, O.P. Pandey, K. Singh, D. Homa, B. Scott, G. Pickrell, A review of bioactive glasses: Their structure, properties, fabrication and apatite formation, Journal of Biomedical Materials Research Part A. 102 (2014) 254–274. https://doi.org/10.1002/jbm.a.34690.
- [29] J.G.C. Wolke, J.M.A. de Blieck-Hogervorst, W.J.A. Dhert, C.P.A.T. Klein, K. de Groot, Studies on the thermal spraying of apatite bioceramics, Journal of Thermal Spray Technology. 1 (1992) 75–82. https://doi.org/10.1007/BF02657021.
- [30] A.L.B. Maçon, T.B. Kim, E.M. Valliant, K. Goetschius, R.K. Brow, D.E. Day, A. Hoppe, A.R. Boccaccini, I.Y. Kim, C. Ohtsuki, T. Kokubo, A. Osaka, M. Vallet-Regí, D. Arcos, L. Fraile, A.J. Salinas, A. V. Teixeira, Y. Vueva, R.M. Almeida, M. Miola, C. Vitale-Brovarone, E. Verné, W. Höland, J.R. Jones, A unified in vitro evaluation for apatite-forming ability of bioactive glasses and their variants, Journal of Materials Science: Materials in Medicine. 26 (2015) 1–10. https://doi.org/10.1007/s10856-015-5403-9.
- [31] V.S. Kattimani, S. Kondaka, K.P. Lingamaneni, Hydroxyapatite—Past, Present, and Future in Bone Regeneration, Bone and Tissue Regeneration Insights. 7 (2016) BTRI.S36138. https://doi.org/10.4137/btri.s36138.
- [32] W. Huang, D.E. Day, K. Kittiratanapiboon, M.N. Rahaman, Kinetics and mechanisms of the conversion of silicate (45S5), borate, and borosilicate glasses to hydroxyapatite in dilute phosphate solutions, Journal of Materials Science: Materials in Medicine. 17 (2006) 583–596. https://doi.org/10.1007/s10856-006-9220-z.
- [33] S. Koutsopoulos, Synthesis and characterization of hydroxyapatite crystals: A review study on the analytical methods, Journal of Biomedical Materials Research. 62 (2002) 600–612. https://doi.org/10.1002/jbm.10280.
- [34] K.S.K. Lin, Y.H. Tseng, Y. Mou, Y.C. Hsu, C.M. Yang, J.C.C. Chan, Mechanistic study of apatite formation on bioactive glass surface using 31P solid-state NMR spectroscopy, Chemistry of Materials. 17 (2005) 4493–4501. https://doi.org/10.1021/cm050654c.
- [35] G.L. de Lange, K. Donath, Interface between bone tissue and implants of solid hydroxyapatite or hydroxyapatite-coated titanium implants, Biomaterials. 10 (1989) 121–125. https://doi.org/10.1016/0142-9612(89)90044-6.
- [36] H. Oonishi, M. Yamamoto, H. Ishimaru, E. Tsuji, S. Kushitani, M. Aono, Y. Ukon, The effect of hydroxyapatite coating on bone growth into porous titanium alloy implants, Journal of Bone and Joint Surgery Series B. 71 (1989) 213–216. https://doi.org/10.1302/0301-620x.71b2.2925737.
- [37] R.I.M. Asri, W.S.W. Harun, M. Samykano, N.A.C. Lah, S.A.C. Ghani, F. Tarlochan, M.R. Raza, Corrosion and surface modification on biocompatible metals: A review, Materials Science and Engineering C. 77 (2017) 1261–1274. https://doi.org/10.1016/j.msec.2017.04.102.
- [38] X.B. Chen, H.Y. Yang, T.B. Abbott, M.A. Easton, N. Birbilis, Corrosion protection of magnesium and its alloys by metal phosphate conversion coatings, Surface Engineering. 30 (2014) 871–879. https://doi.org/10.1179/1743294413Y.0000000235.
- [39] Y. Dou, S. Cai, X. Ye, G. Xu, K. Huang, X. Wang, M. Ren, 45S5 bioactive glass-ceramic coated AZ31 magnesium alloy with improved corrosion resistance, Surface and Coatings Technology. 228 (2013) 154–161. https://doi.org/10.1016/j.surfcoat.2013.04.022.

- [40] C. Vasilescu, P. Drob, E. Vasilescu, I. Demetrescu, D. Ionita, M. Prodana, S.I. Drob, Characterisation and corrosion resistance of the electrodeposited hydroxyapatite and bovine serum albumin/hydroxyapatite films on Ti-6Al-4V-1Zr alloy surface, Corrosion Science. 53 (2011) 992–999. https://doi.org/10.1016/j.corsci.2010.11.033.
- [41] S. Lopez-Esteban, E. Saiz, S. Fujino, T. Oku, K. Suganuma, A.P. Tomsia, Bioactive glass coatings for orthopedic metallic implants, Journal of the European Ceramic Society. 23 (2003) 2921–2930. https://doi.org/10.1016/S0955-2219(03)00303-0.
- [42] A. Pazo, E. Saiz, A.P. Tomsia, SILICATE COATINGS ON Ti-BASED IMPLANTS, Acta Materialia. 46 (1998) 2551–2558.
- [43] L. Peddi, R.K. Brow, R.F. Brown, Bioactive borate glass coatings for titanium alloys, Journal of Materials Science: Materials in Medicine. 19 (2008) 3145–3152. https://doi.org/10.1007/s10856-008-3419-0.
- [44] S. Shen, S. Cai, G. Xu, H. Zhao, S. Niu, R. Zhang, Influence of heat treatment on bond strength and corrosion resistance of sol-gel derived bioglass-ceramic coatings on magnesium alloy, Journal of the Mechanical Behavior of Biomedical Materials. 45 (2015) 166–174. https://doi.org/10.1016/j.jmbbm.2015.02.005.
- [45] J.M. Gomez-Vega, E. Saiz, A.P. Tomsia, T. Oku, K. Suganuma, G.W. Marshall, S.J. Marshall, Novel Bioactive Functionally Graded Coatings on Ti6Al4V, Advanced Materials. 12 (2000) 894–898. https://doi.org/10.1002/1521-4095(200006)12:12<894::AID-ADMA894>3.0.CO;2-4.
- [46] H. Li, B.S. Ng, K.A. Khor, P. Cheang, T.W. Clyne, Raman spectroscopy determination of phases within thermal sprayed hydroxyapatite splats and subsequent *in vitro* dissolution examination, Acta Materialia. 52 (2004) 445–453. https://doi.org/10.1016/j.actamat.2003.09.046.
- [47] S. Milton, An introduction to thermal spraying, Corrosion Management. 2017-Novem (2017) 20–23.
- [48] N. Moritz, S. Rossi, E. Vedel, T. Tirri, H. Ylänen, H. Aro, T. Närhi, Implants coated with bioactive glass by CO₂-laser, an in vivo study, Journal of Materials Science: Materials in Medicine. 15 (2004) 795–802. https://doi.org/10.1023/B:JMSM.0000032820.50983.c1.
- [49] M. Krzyzanowski, S. Bajda, Y. Liu, A. Triantaphyllou, W. Mark Rainforth, M. Glendenning, 3D analysis of thermal and stress evolution during laser cladding of bioactive glass coatings, Journal of the Mechanical Behavior of Biomedical Materials. 59 (2016) 404–417. https://doi.org/10.1016/j.jmbbm.2016.02.023.
- [50] P.H. Kuo, S.S. Joshi, X. Lu, Y.H. Ho, Y. Xiang, N.B. Dahotre, J. Du, Laser coating of bioactive glasses on bioimplant titanium alloys, International Journal of Applied Glass Science. 10 (2019) 307–320. https://doi.org/10.1111/ijag.12642.
- [51] R. Li, Z. Li, J. Huang, Y. Zhu, Dilution effect on the formation of amorphous phase in the laser cladded Ni-Fe-B-Si-Nb coatings after laser remelting process, Applied Surface Science. 258 (2012) 7956–7961. https://doi.org/10.1016/j.apsusc.2012.04.144.
- [52] A. V. Gayathri Devi, V. Rajendran, N. Rajendran, Structure, solubility and bioactivity in TiO<sub>2<\sub>-doped phosphate-based bioglasses and glass-ceramics, Materials Chemistry and Physics. 124 (2010) 312–318. https://doi.org/10.1016/j.matchemphys.2010.06.038.

- [53] A.A. El-Kheshen, F.A. Khaliafa, E.A. Saad, R.L. Elwan, Effect of Al2O3addition on bioactivity, thermal and mechanical properties of some bioactive glasses, Ceramics International. 34 (2008) 1667–1673. https://doi.org/10.1016/j.ceramint.2007.05.016.
- [54] M.N. Rahaman, D.E. Day, B. Sonny Bal, Q. Fu, S.B. Jung, L.F. Bonewald, A.P. Tomsia, Bioactive glass in tissue engineering, Acta Biomaterialia. 7 (2011) 2355–2373. https://doi.org/http://dx.doi.org/10.1016/j.actbio.2011.03.016.
- [55] M.D. O'Donnell, R.G. Hill, M.D.O. Donnell, R.G. Hill, Influence of strontium and the importance of glass chemistry and structure when designing bioactive glasses for bone regeneration, Acta Biomaterialia. 6 (2010) 2382–2385. https://doi.org/http://dx.doi.org/10.1016/j.actbio.2010.01.006.
- [56] L.A. Strobel, N. Hild, D. Mohn, W.J. Stark, A. Hoppe, U. Gbureck, R.E. Horch, U. Kneser, A.R. Boccaccini, Novel strontium-doped bioactive glass nanoparticles enhance proliferation and osteogenic differentiation of human bone marrow stromal cells, Journal of Nanoparticle Research. 15 (2013). https://doi.org/10.1007/s11051-013-1780-5.
- [57] M. Dziadek, B. Zagrajczuk, E. Menaszek, A. Wegrzynowicz, J. Pawlik, K. Cholewa-Kowalska, Gel-derived SiO₂-CaO-P₂O₅ bioactive glasses and glass-ceramics modified by SrO addition, Ceramics International. 42 (2016) 5842–5857. https://doi.org/10.1016/j.ceramint.2015.12.128.
- [58] A.M. Abdelghany, M.A. Ouis, M.A. Azooz, H.A. Elbatal, G.T. El-Bassyouni, Role of SrO on the bioactivity behavior of some ternary borate glasses and their glass ceramic derivatives, Spectrochimica Acta Part A: Molecular and Biomolecular Spectroscopy. 152 (2016) 126–133. https://doi.org/10.1016/j.saa.2015.07.072.
- [59] C. Steffi, Z. Shi, C.H. Kong, W. Wang, Modulation of osteoclast interactions with orthopaedic biomaterials, Journal of Functional Biomaterials. 9 (2018). https://doi.org/10.3390/jfb9010018.
- [60] M. Bellantone, H.D. Williams, L.L. Hench, Broad-Spectrum Bactericidal Activity of Ag₂O-Doped Bioactive Glass, Antimicrobial Agent And Chemotherapy. 46 (2002) 1940–1945. https://doi.org/10.1128/AAC.46.6.1940.
- [61] N. Zhu, X. Chatzistavrou, P. Papagerakis, L. Ge, M. Qin, Y. Wang, Silver-Doped Bioactive Glass/Chitosan Hydrogel with Potential Application in Dental Pulp Repair, ACS Biomaterials Science and Engineering. 5 (2019) 4624–4633. https://doi.org/10.1021/acsbiomaterials.9b00811.
- [62] R.F. Brown, M.N. Rahaman, A.B. Dwilewicz, W. Huang, D.E. Day, Y. Li, B.S. Bal, Effect of borate glass composition on its conversion to hydroxyapatite and on the proliferation of MC3T3-E1 cells, Journal of Biomedical Materials Research - Part A. 88 (2009) 392–400. https://doi.org/10.1002/jbm.a.31679.
- [63] M. Brink, T. Turunen, R.P. Happonen, A. Yli-Urpo, Compositional dependence of bioactivity of glasses in the system Na2O- K2O-MgO-Cao-B2O3-P2O5-SiO2, Journal of Biomedical Materials Research. 37 (1997) 114–121. https://doi.org/10.1002/(SICI)1097-4636(199710)37:1<114::AID-JBM14>3.0.CO;2-G.
- [64] A. Hoppe, N.S. Güldal, A.R. Boccaccini, A review of the biological response to ionic dissolution products from bioactive glasses and glass-ceramics, Biomaterials. 32 (2011) 2757–2774. https://doi.org/10.1016/j.biomaterials.2011.01.004.

- [65] W. Liang, M.N. Rahaman, D.E. Day, N.W. Marion, G.C. Riley, J.J. Mao, Bioactive borate glass scaffold for bone tissue engineering, Journal of Non-Crystalline Solids. 354 (2008) 1690–1696. https://doi.org/10.1016/j.jnoncrysol.2007.10.003.
- [66] Q. Fu, M.N. Rahaman, B.S. Bal, L.F. Bonewald, K. Kuroki, R.F. Brown, Silicate, borosilicate, and borate bioactive glass scaffolds with controllable degradation rate for bone tissue engineering applications. II. In vitro and in vivo biological evaluation, Journal of Biomedical Materials Research Part A. 95 (2010) 172–179. https://doi.org/10.1002/jbm.a.32823.
- [67] Q. Fu, M.N. Rahaman, B.S. Bal, W. Huang, D.E. Day, Preparation and bioactive characteristics of a porous 13-93 glass, and fabrication into the articulating surface of a proximal tibia, Journal of Biomedical Materials Research Part A. 82 (2007) 222–229. https://doi.org/10.1002/jbm.a.31156.
- [68] H. Fu, Q. Fu, N. Zhou, W. Huang, M.N. Rahaman, D. Wang, X. Liu, In vitro evaluation of borate-based bioactive glass scaffolds prepared by a polymer foam replication method, Materials Science and Engineering: C. 29 (2009) 2275–2281. https://doi.org/http://dx.doi.org/10.1016/j.msec.2009.05.013.
- [69] S. Foppiano, S.J. Marshall, G.W. Marshall, E. Saiz, A.P. Tomsia, Bioactive glass coatings affect the behavior of osteoblast-like cells, Acta Biomaterialia. 3 (2007) 765–771. https://doi.org/10.1016/j.actbio.2007.02.011.
- [70] M. Ren, X. Lu, L. Deng, P.H. Kuo, J. Du, B2O3/SiO2 substitution effect on structure and properties of Na2O-CaO-SrO-P2O5-SiO2 bioactive glasses from molecular dynamics simulations, Physical Chemistry Chemical Physics. 20 (2018) 14090–14104. https://doi.org/10.1039/c7cp08358k.
- [71] X. Yang, L. Zhang, X. Chen, X. Sun, G. Yang, X. Guo, H. Yang, C. Gao, Z. Gou, Incorporation of B₂O₃ in CaO-SiO₂-P₂O₅ bioactive glass system for improving strength of low-temperature co-fired porous glass ceramics, Journal of Non-Crystalline Solids. 358 (2012) 1171–1179. https://doi.org/10.1016/j.jnoncrysol.2012.02.005.
- [72] K. Xie, L. Zhang, X. Yang, X. Wang, G. Yang, L. Zhang, H. Shao, Y. He, J. Fu, Z. Gou, Preparation and characterization of low temperature heat-treated 45s5 bioactive glass-ceramic analogues, Biomedical Glasses. 1 (2015) 80–92. https://doi.org/10.1515/bglass-2015-0008.
- [73] D. Bellucci, V. Cannillo, A. Sola, Coefficient of thermal expansion of bioactive glasses: Available literature data and analytical equation estimates, Ceramics International. 37 (2011) 2963–2972. https://doi.org/10.1016/j.ceramint.2011.05.048.
- [74] S. Fujino, H. Tokunaga, E. Saiz, A.P. Tomsia, Fabrication and Characterization of Bioactive Glass Coatings on Co-Cr Implant Alloys, Materials Transactions. 45 (2004) 1147–1151.
- [75] M.D. O'Donnell, Predicting bioactive glass properties from the molecular chemical composition: Glass transition temperature, Acta Biomaterialia. 7 (2011) 2264–2269. https://doi.org/10.1016/j.actbio.2011.01.021.
- [76] J.M. Gomez-Vega, E. Saiz, A.P. Tomsia, G.W. Marshall, S.J. Marshall, Bioactive glass coatings with hydroxyapatite and Bioglass® particles on Ti-based implants. 1. Processing, Biomaterials. 21 (2000) 105–111. https://doi.org/http://dx.doi.org/10.1016/S0142-9612(99)00131-3.

- [77] J.C. Mauro, Decoding the glass genome, Current Opinion in Solid State and Materials Science. 22 (2018) 58–64. https://doi.org/10.1016/j.cossms.2017.09.001.
- [78] Z. Liu, Perspective on Materials Genome®, Chinese Science Bulletin. 59 (2014) 1619–1623. https://doi.org/10.1007/s11434-013-0072-x.
- [79] J.C. Mauro, A. Tandia, K.D. Vargheese, Y.Z. Mauro, M.M. Smedskjaer, Accelerating the Design of Functional Glasses through Modeling, Chemistry of Materials. 28 (2016) 4267–4277. https://doi.org/10.1021/acs.chemmater.6b01054.
- [80] A. Pedone, M.C. Menziani, Molecular Dynamics Simulations of Disordered Materials, Molecular Dynamics Simulations Disordered Materials. 215 (2015) 113–135. https://doi.org/10.1007/978-3-319-15675-0.
- [81] D.R. Cassar, A.C.P.L.F. de Carvalho, E.D. Zanotto, Predicting glass transition temperatures using neural networks, Acta Materialia. 159 (2018) 249–256. https://doi.org/10.1016/j.actamat.2018.08.022.
- [82] W. Liu, C. Cao, Artificial neural network prediction of glass transition temperature of polymers, Colloid and Polymer Science. 287 (2009) 811–818. https://doi.org/10.1007/s00396-009-2035-y.
- [83] H. el Kadi, Y. Al-Assaf, Prediction of the fatigue life of unidirectional glass fiber/epoxy composite laminae using different neural network paradigms, Composite Structures. 55 (2002) 239–246. https://doi.org/10.1016/S0263-8223(01)00152-0.
- [84] X. Lu, J. Du, Quantitative structure-property relationship (QSPR) analysis of calcium aluminosilicate glasses based on molecular dynamics simulations, Journal of Non-Crystalline Solids. 530 (2020). https://doi.org/10.1016/j.jnoncrysol.2019.119772.
- [85] X. Lu, L. Deng, S. Gin, J. Du, Quantitative Structure-Property Relationship (QSPR) Analysis of ZrO 2 -Containing Soda-Lime Borosilicate Glasses, Journal of Physical Chemistry B. 123 (2019) 1412–1422. https://doi.org/10.1021/acs.jpcb.8b11108.
- [86] S. Gin, M. Wang, N. Bisbrouck, M. Taron, X. Lu, L. Deng, F. Angeli, T. Charpentier, J.-M. Delaye, J. Du, M. Bauchy, Can a simple topological-constraints-based model predict the initial dissolution rate of borosilicate and aluminosilicate glasses?, Npj Materials Degradation. 4 (2020). https://doi.org/10.1038/s41529-020-0111-4.
- [87] C. Hermansen, J.C. Mauro, Y. Yue, A model for phosphate glass topology considering the modifying ion sub-network, Journal of Chemical Physics. 140 (2014). https://doi.org/10.1063/1.4870764.
- [88] G. Lusvardi, G. Malavasi, L. Menabue, M.C. Menziani, A. Pedone, U. Segre, Density of multicomponent silica-based potential bioglasses: Quantitative structure-property relationships (QSPR) analysis, Journal of the European Ceramic Society. 27 (2007) 499–504. https://doi.org/10.1016/j.jeurceramsoc.2006.04.067.
- [89] L. Linati, G. Lusvardi, G. Malavasi, L. Menabue, M.C. Menziani, P. Mustarelli, U. Segre, Qualitative and quantitative structure-property relationships analysis of multicomponent potential bioglasses, Journal of Physical Chemistry B. 109 (2005) 4989–4998. https://doi.org/10.1021/jp046631n.

- [90] J. Du, X. Lu, S. Gin, J.-M. Delaye, L. Deng, M. Taron, N. Bisbrouck, M. Bauchy, J.D. Vienna, Predicting the Dissolution Rate of Borosilicate Glasses by using QSPR Analysis based on Molecular Dynamics Simulations Journal:, Journal of the American Ceramic Society. (2021) 4– 11.
- [91] G. Lusvardi, G. Malavasi, F. Tarsitano, L. Menabue, M.C. Menziani, A. Pedone, Quantitative structure-property relationships of potentially bioactive fluoro phospho-silicate glasses, Journal of Physical Chemistry B. 113 (2009) 10331–10338. https://doi.org/10.1021/jp809805z.
- [92] A.R. Katritzky, V.S. Lobanov, M. Karelson, QSPR: The Correlation and Quantitative Prediction of Chemical and Physical Properties from Structure, 1995.
- [93] M. Montazerian, E.D. Zanotto, J.C. Mauro, Model-driven design of bioactive glasses: from molecular dynamics through machine learning, International Materials Reviews. 65 (2020) 297–321. https://doi.org/10.1080/09506608.2019.1694779.
- [94] Y. Xiang, J. Du, Effect of strontium substitution on the structure of 45S5 bioglasses, Chemistry of Materials. 23 (2011) 2703–2717. https://doi.org/10.1021/cm102889q.
- [95] X. Lu, L. Deng, P.H. Kuo, M. Ren, I. Buterbaugh, J. Du, Effects of boron oxide substitution on the structure and bioactivity of SrO-containing bioactive glasses, Journal of Materials Science. 52 (2017) 8793–8811. https://doi.org/10.1007/s10853-017-0836-9.
- [96] S. Lopez-Esteban, C.F. Gutierrez-Gonzalez, L. Gremillard, E. Saiz, A.P. Tomsia, Interfaces in graded coating on titaniu-based implants, Journal of Biomedical Materials Research Part A. 88 (2009) 1010–1021. https://doi.org/10.1038/jid.2014.371.
- [97] J.M. Tainio, D.A.A. Salazar, A. Nommeots-Nomm, C. Roiland, B. Bureau, D.R. Neuville, D.S. Brauer, J. Massera, Structure and in vitro dissolution of Mg and Sr containing borosilicate bioactive glasses for bone tissue engineering, Journal of Non-Crystalline Solids. 533 (2020) 119893. https://doi.org/10.1016/j.jnoncrysol.2020.119893.
- [98] O. Rodriguez, D.J. Curran, M. Papini, L.M. Placek, A.W. Wren, E.H. Schemitsch, P. Zalzal, M.R. Towler, Characterization of silica-based and borate-based, titanium-containing bioactive glasses for coating metallic implants, Journal of Non-Crystalline Solids. 433 (2016) 95–102. https://doi.org/http://dx.doi.org/10.1016/j.jnoncrysol.2015.09.026.
- [99] W. Jia, H. Hu, A. Li, H. Deng, C.L. Hogue, J.C. Mauro, C. Zhang, Q. Fu, Glass-activated regeneration of volumetric muscle loss, Acta Biomaterialia. 103 (2020) 306–317. https://doi.org/10.1016/j.actbio.2019.12.007.
- [100] Y. Yue, M.I. Tuheen, J. Du, Borosilicate Glasses, in: M. Pomeroy (Ed.), Encyclopedia of Materials: Technical Ceramics and Glasses, Elsevier, Oxford, 2021: pp. 519–539. https://doi.org/https://doi.org/10.1016/B978-0-12-818542-1.00098-9.
- [101] R.K. Brow, S.K. Saha, J.I. Goldstein, Interfacial reactions between titaniuh and borate glass, MRS Online Proceedings Library Archive. 314 (1993) 77–82.
- [102] S. Plimpton, Fast Parallel Algorithms for Short-Range Molecular Dynamics, 1995. http://www.cs.sandia.gov/~sjplimp/main.html.

- [103] A. Yao, D. Wang, W. Huang, Q. Fu, M.N. Rahaman, D.E. Day, In vitro bioactive characteristics of borate-based glasses with controllable degradation behavior, Journal of the American Ceramic Society. 90 (2007) 303–306. https://doi.org/10.1111/j.1551-2916.2006.01358.x.
- [104] R.F. Brown, M.N. Rahaman, A.B. Dwilewicz, W. Huang, D.E. Day, Y. Li, B.S. Bal, Effect of borate glass composition on its conversion to hydroxyapatite and on the proliferation of MC3T3-E1 cells, Journal of Biomedical Materials Research - Part A. 88 (2009) 392–400. https://doi.org/10.1002/jbm.a.31679.
- [105] L. Deng, J. Du, Development of effective empirical potentials for molecular dynamics simulations of the structures and properties of boroaluminosilicate glasses, Journal of Non-Crystalline Solids. 453 (2016) 177–194. https://doi.org/10.1016/j.jnoncrysol.2016.09.021.
- [106] L. Deng, J. Du, Development of boron oxide potentials for computer simulations of multicomponent oxide glasses, Journal of the American Ceramic Society. 102 (2019) 2482–2505. https://doi.org/10.1111/jace.16082.
- [107] L. Deng, X. Lu, J.D. Vienna, J. Du, Structures of vanadium containing silicate and borosilicate glasses: vanadium potential development and MD simulations, Journal of Non-Crystalline Solids. 575 (2022) 121223. https://doi.org/10.1016/j.jnoncrysol.2021.121223.
- [108] A.P. Thompson, S.J. Plimpton, W. Mattson, General formulation of pressure and stress tensor for arbitrary many-body interaction potentials under periodic boundary conditions, Journal of Chemical Physics. 131 (2009). https://doi.org/10.1063/1.3245303.
- [109] R. Hill, The elastic behaviour of a crystalline aggregate, Proceedings of the Physical Society. Section A. 65 (1952) 349–354. https://doi.org/10.1088/0370-1298/65/5/307.
- [110] J.C. Mauro, P.K. Gupta, R.J. Loucks, Composition dependence of glass transition temperature and fragility. II. A topological model of alkali borate liquids, Journal of Chemical Physics. 130 (2009). https://doi.org/10.1063/1.3152432.
- [111] L.L. Hench, J.R. Jones, P. Sepulveda, Bioactive materials for tissue engineering scaffolds, in: Future Strategies for Tissue and Organ Replacement, World Scientific, 2002: pp. 3–24.
- [112] A. Winkelmann, O. Schott, Uber thermische Widerstandscoefficienten verschiedener Glaser in ihrer Abhangigkeit von der chemischen Zusammensetzung, Annalen Der Physik. 287 (1894) 730– 746.
- [113] S. English, W.E.S. Turner, RELATIONSHIP BETWEEN CHEMICAL COMPOSITION AND THE THERMAL EXPANSION OF GLASSES, Journal of American Cer. 10 (1927) 551–560.
- [114] F.P. Hall, THE INFLUENCE OF CHEMICAL COMPOSITION ON THE PHYSICAL PROPERTIES OF GLAZES*, J. Am. Ceram. Soc. 13 (1930) 182–199.
- [115] M.J. Jackson, B. Mills, Thermal expansion of alumino-alkalisilicate and alumino-borosilicate glasses--comparison of empirical models, Journal of Materials Science Letters. 16 (1997) 1264–1266.
- [116] S. Lopez-esteban, E. Saiz, S. Fujino, T. Oku, K. Suganuma, A.P. Tomsia, Bioactive glass coatings for orthopedic metallic implants, Journal of European Ceramic Society. 23 (2003) 2921–2930. https://doi.org/10.1016/S0955-2219(03)00303-0.

- [117] Y. Yu, B. Stevensson, M. Edén, Medium-range structural organization of phosphorus-bearing borosilicate glasses revealed by sdvanced solid-state NMR experiments and MD simulations: consequences of B/Si substitutions, J. Phys. Chem. B. 121 (2017) 9737–9752. https://doi.org/10.1021/acs.jpcb.7b06654.
- [118] B. Stevensson, Y. Yu, M. Edén, Structure-composition trends in multicomponent borosilicate-based glasses deduced from molecular dynamics simulations with improved B-O and P-O force fields, Phys. Chem. Chem. Phys. 20 (2018) 8192–8209. https://doi.org/10.1039/c7cp08593a.
- [119] Y. Yu, M. Eden, Structure composition relationships of bioactive borophosphosilicate glasses probed by multinuclear 11B, 29Si, and 31P solid state NMR, RSC Adv. 6 (2016) 101288–101303. https://doi.org/10.1039/c6ra15275a.
- [120] X. Lu, L. Deng, C. Huntley, M. Ren, P.H. Kuo, T. Thomas, J. Chen, J. Du, Mixed Network Former Effect on Structure, Physical Properties, and Bioactivity of 45S5 Bioactive Glasses: An Integrated Experimental and Molecular Dynamics Simulation Study, J. Phys. Chem. B. 122 (2018) 2564–2577. https://doi.org/10.1021/acs.jpcb.7b12127.
- [121] X. Lu, J. Kolzow, R.R. Chen, J. Du, Effect of solution condition on hydroxyapatite formation in evaluating bioactivity of B2O3 containing 45S5 bioactive glasses, Bioact. Mater. 4 (2019) 207–214. https://doi.org/10.1016/j.bioactmat.2019.05.002.

Tables:

Table 1. Glass compositions (in mol %), B/Si ratio, percentage of NBO and the final densities from MD of bioactive glass 6P55, and 6P55 with B₂O₃/SiO₂ and 6P55 with BO_{3/2}/SiO₂ substitutions

B ₂ O ₃ /SiO ₂ substitution (1:2-gf-sub)										
Glass name	SiO ₂	B_2O_3	P ₂ O ₅	MgO	CaO	Na ₂ O	K ₂ O	Density (g/cm ³)	B/Si Ratio	NBO %
6P55	54.5	0	2.5	12.7	16.1	11.6	2.6	2.674±0.004	0.0	54.3
6P55_5%B ₂ O ₃	49.5	5	2.5	12.7	16.1	11.6	2.6	2.568 ± 0.007	0.202	49.9
6P55_10%B ₂ O ₃	44.5	10	2.5	12.7	16.1	11.6	2.6	2.537 ± 0.003	0.449	49.8
6P55_15%B ₂ O ₃	39.5	15	2.5	12.7	16.1	11.6	2.6	2.509 ± 0.002	0.759	44.8
BO _{3/2} /SiO ₂ substitution (1:1-gf-sub)										
Glass name	SiO ₂	BO _{1.5}	P ₂ O ₅	MgO	CaO	Na ₂ O	K ₂ O	Density (g/cm ³)		
6P55_5%BO _{3/2}	49.5	5	2.5	12.7	16.1	11.6	2.6	2.566 ± 0.007	0.101	50.6
6P55_10%BO _{3/2}	44.5	10	2.5	12.7	16.1	11.6	2.6	2.568 ± 0.004	0.225	53.3
6P55_15% BO _{3/2}	39.5	15	2.5	12.7	16.1	11.6	2.6	2.564 ± 0.009	0.380	56.0

Table 2 Partial atomic charge and pair-wise potential parameters [106, 107]

Atomio noir	Buckingham potential parameters						
Atomic pair	A_{ij}	$ ho_{ij}$	C_{ij}				
O ^{-1.2} -O ^{-1.2}	2029.2204	0.343645	192.58				
Si ^{2.4} -O ^{-1.2}	13702.9050	0.193817	54.681				
B ^{1.8} -O ^{-1.2}	Compositional dependent [106]	0.171271	28.500				
$Mg^{1.2}$ - $O^{-1.2}$ [107]	7063.4907	0.2109	19.210				
$Ca^{1.2}-O^{-1.2}$	7747.1834	0.252623	93.109				
Na ^{0.6} -O ^{-1.2}	4383.7555	0.243838	30.700				
K ^{0.6} -O ^{-1.2}	20526.9720	0.233708	51.489				

Table 3 Bond distance of $B^{[3]}$ -O and $B^{[4]}$ -O in B_2O_3/SiO_2 and $BO_{3/2}/SiO_2$ substituted 6P55 series

	B-O pair	5%	10%	15%
1:2-gf-sub	B ^[3] -O (Å)	1.42	1.39	1.39
	B ^[4] -O (Å)	1.51	1.49	1.49
1:1-gf-sub	B ^[3] -O (Å)	1.45	1.41	1.38
	B ^[4] -O (Å)	1.53	1.51	1.45

Table 4 Percentage of $B^{[3]}$ and $B^{[4]}$ in B_2O_3/SiO_2 and $BO_3/2/SiO_2$ substituted 6P55 series

	Boron CN	5%	10%	15%
1:2-gf-sub	$B^{[3]}$	38.94±2.1	75.93±1.0	74.73±1.3
	$\mathrm{B}^{[4]}$	61.06±2.1	24.07±1.0	25.17±1.3
1:1-gf-sub	$\mathbf{B}^{[3]}$	26.93±3.1	48.64±1.0	81.46±1.7
	B ^[4]	73.07±3.1	51.36±1.0	18.54±1.7

Table 5 Summary of Q_n species change of Si, P and B_n species for B in 6P55 with B₂O₃ substitution

	Si		P		В	
1:1 gf sub	No significan	nt change	Q₀↑	$Q_1 \downarrow Q_2 \downarrow$	$B_0\uparrow B_1\uparrow B_2\uparrow$	B₃↓ B₄↓
1:2 gf sub	$Q_1 \downarrow Q_2 \downarrow$	Q4↑	$Q_{o}\downarrow Q_{1}\downarrow$	Q2↑ Q3↑	B₁↑B₂↑	B₄↓

Table 6 Proportionality factor of oxides from empirical models

Oxides	$lpha_i$ of oxides from the models							
	Winkelmann & Schott	English &Turner	Hall's	Gilard & Dubrul				
	(W.S)[112]	(E.T)[113]	(H)[114]	(G.D)[115]				
SiO ₂	2.67	0.5	1.4	0.4				
B_2O_3	0.33	-6.53	2.0	-4 + 0.1p				
P ₂ O ₅	6.67							
*P ₂ O ₅ [111]	0.35	0.24	0.36	0.59				
MgO	0.33	4.50	2.0	0				
CaO	16.67	16.30	15.0	7.5 + 0.35p				
Na ₂ O	33.33	41.60	38.0	51-0.33p				
K ₂ O	28.33	39.00	30.0	42-0.33 <i>p</i>				

Figure Captions:

- Figure 1. Snapshot of structure model of 6P55_10%B₂O₃ bioactive glass from MD simulation. Left panel shows the whole simulation cell with around 10,000 atoms with simulation cell of 51.1x51.1x51.1 Å³ and the right panel shows zoomed in image of the glass network structure consisting of SiO₄, PO₄, BO₃ and BO₄ structural units.
- Figure 2 TDF (solid line) and CN (dash line) of (a) Si-O and (b) P-O of 6P55 (para represents the three parallel simulations for each composition)
- Figure 3 TDF-CN of (a) Si-O, (b) B-O and (c) P-O of 6P55 with 5%, 10% and 15% B₂O₃/SiO₂ substitution
- Figure 4 TDF-CN of (a) Si-O, (b) B-O and (c) P-O of 6P55 with 5%, 10% and 15% BO_{3/2}/SiO₂ substitution
- Figure 5 PDF of B-O and the deconvolution of $B^{[3]}$ -O and $B^{[4]}$ -O of 6P55 with (a) 5%, (b)10% and (c)15% B_2O_3/SiO_2 substitutions
- Figure 6 PDF of B-O and the deconvolution of $B^{[3]}$ -O and $B^{[4]}$ -O of 6P55 with (a) 5%, (b)10% and (c)15% BO_{3/2}/SiO₂substitutions
- Figure 7 BAD of (a) ∠Si-O-Si, (b) ∠Si-O-B and (c) ∠Si-O-P of 1:2-gf-sub series
- Figure 8 BAD of (a) ∠Si-O-Si, (b) ∠Si-O-B and (c) ∠Si-O-P of 1:1-gf-sub series
- Figure 9 BAD of (a) \angle Si-O-B^[3] and (b) \angle Si-O-B^[4] in 1:2-gf-sub
- Figure 10 BAD of (a) \angle Si-O-B^[3] and (b) \angle Si-O-B^[4] in 1:1-gf-sub
- Figure 11 SiO_n species distribution of (a) 1:2-gf-sub, (b) 1:1-gf-sub and 6P55
- Figure 12 PQ_n species distribution of (a) 1:2-gf-sub and (b) 1:1-gf-sub vs 6P55
- Figure 13 B_n species distribution of (a) 1:2-gf-sub and (b) 1:1-gf-sub
- Figure 14 Snapshot of (a) 1:1-gf-sub 5% glass. Local structure of (b) PQ₀ from a single PO₄ with 4 NBOs, and (c) PQ₃ from a PO₄ corner-sharing with SiO₄ and BO₄ tetrahedrons. (d) B₄ from a BO₄ tetrahedron corner-sharing with PO₄ and SiO₄ tetrahedrons. (e) B₂ and (f) B₁ that composed by BO₃ units.
- Figure 15 (a) T_g fitting of 6P55 and (b) T_g of 6P55, B₂O₃/SiO₂ and BO_{3/2}/SiO₂ substituted series
- Figure 16 (a) CTE fitting for 6P55 with 10% $BO_{3/2}/SiO_2$ and (b) CTE of 6P55 and B_2O_3/SiO_2 and $BO_{3/2}/SiO_2$ substituted 6P55 series
- Figure 17 (a) Bulk modulus, (b) shear modulus and (c) Young's modulus of 6P55 and B₂O₃/SiO₂ and BO_{3/2}/SiO₂ substituted 6P55 series
- Figure 18 (a) Network connectivity (Solid) and T_g (hollow) (b) Snapshot of $B_1^{[3]}$ in 15%BO_{3/2}/SiO₂ (c) B_n of 1:2-gf-sub (green) and 1:1-gf-sub (black) and (d) SiQ_n of 6P55 (red), 1:2-gf-sub (green) and 1:1-gf-sub (black)

- Figure 19 B^[3] and B^[4] of **(a)** 1:1-gf-sub series and **(b)** 1:2-gf-sub from 498K to 2298K. **(c)** Snapshot of $B_2^{[3]}$ and **(d)** $B_3^{[4]}$ from MD simulations
- Figure 20 B_n species of (a) 5%, (b) 10% and (c) 15% of 1:1-gf-sub-series; and (d) 5%, (e) 10% and (f) 15% 1:2-gf-sub-series from 498K to 2298K
- Figure 21 CTE of 6P55 and (a) 1:2-gf-sub and (b) 1:1-gf-sub derived from different models. The gray circle represents the CTE of 6P55 as the reference point
- Figure 22 Network connectivity vs. (a) Bulk modulus (b) Shear modulus and (c) Young's Modulus of 1:2-gf-sub and 1:1-gf-sub glasses

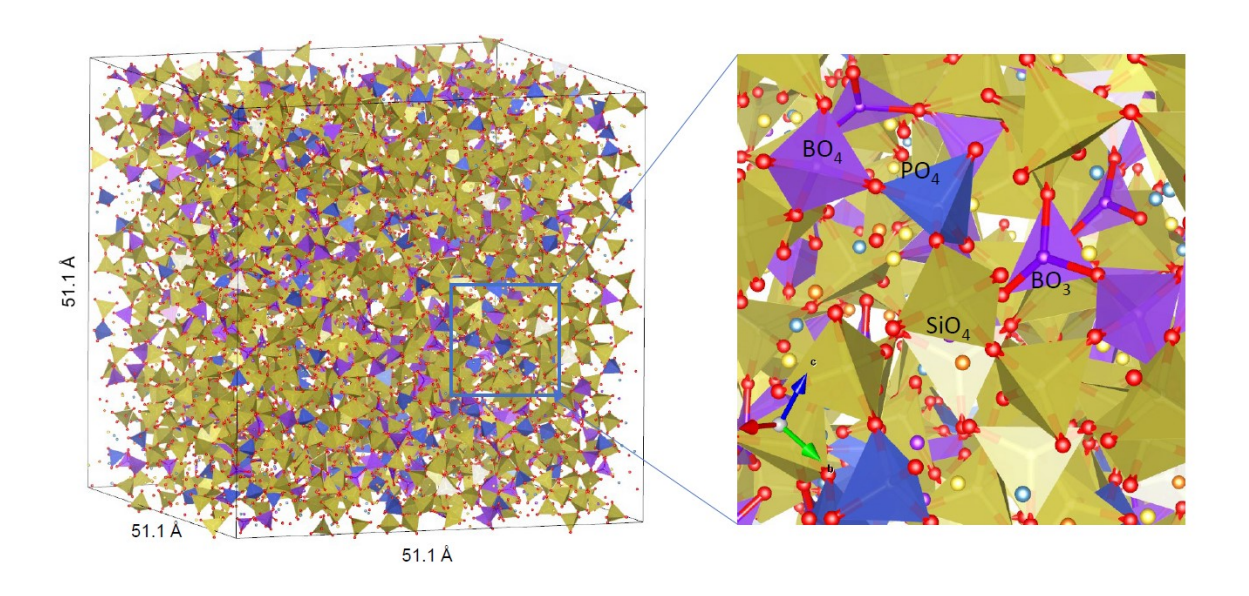


Figure 1. Snapshot of structure model of 6P55_10%B₂O₃ bioactive glass from MD simulation. Left panel shows the whole simulation cell with around 10,000 atoms with simulation cell of 51.1x51.1x51.1 Å³ and the right panel shows zoomed in image of the glass network structure consisting of SiO₄, PO₄, BO₃ and BO₄ structural units.

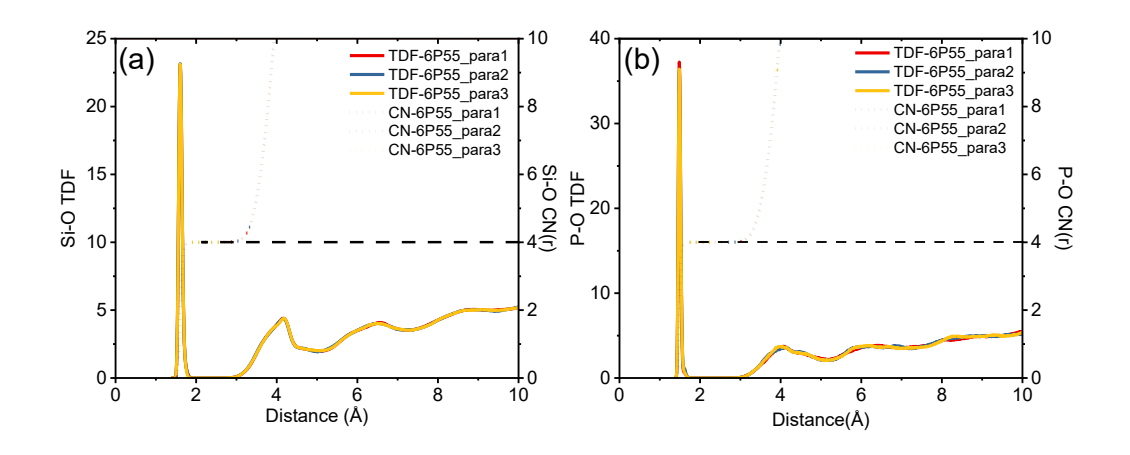


Figure 2 TDF (solid line) and CN (dash line) of (a) Si-O and (b) P-O of 6P55 (para represents the three parallel simulations for each composition)

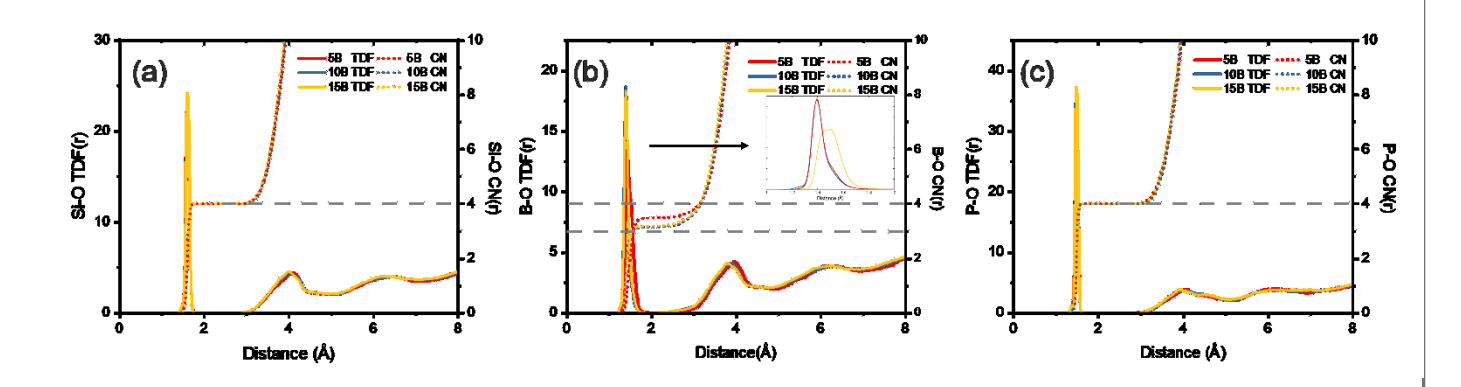


Figure 3 TDF-CN of (a) Si-O, (b) B-O and (c) P-O of 6P55 with 5%, 10% and 15% B₂O₃/SiO₂ substitution

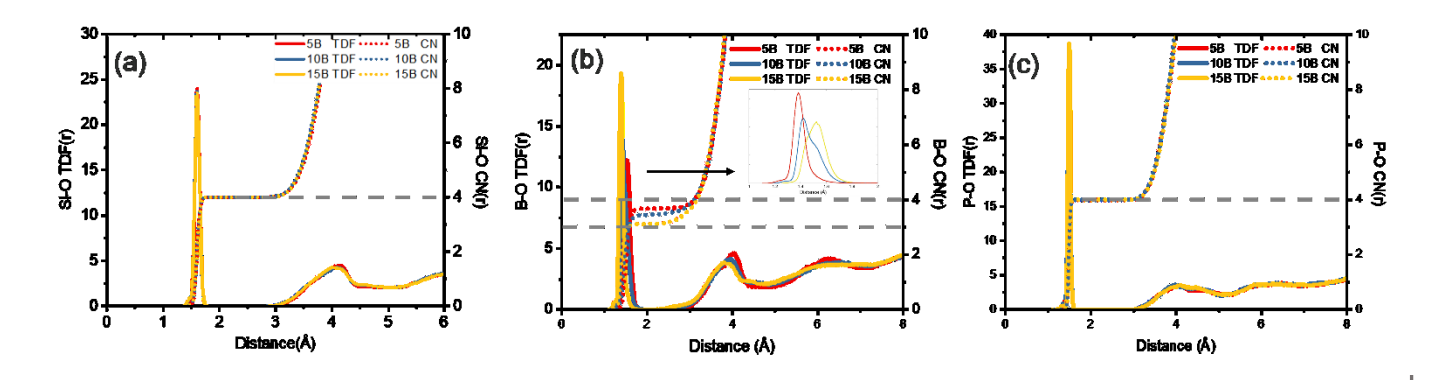


Figure 4 TDF-CN of (a) Si-O, (b) B-O and (c) P-O of 6P55 with 5%, 10% and 15% BO_{3/2}/SiO₂ substitution

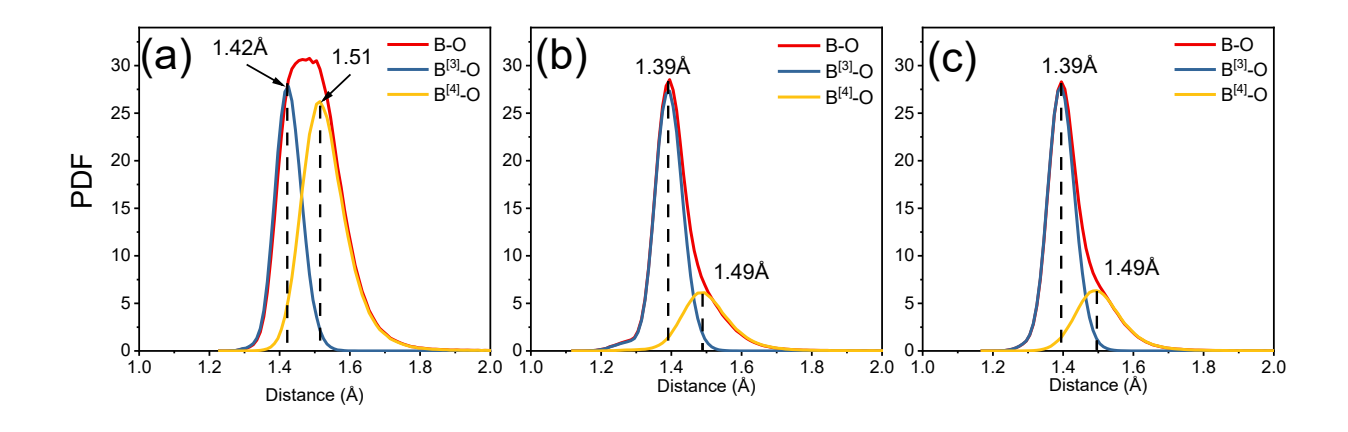


Figure 5 PDF of B-O and the deconvolution of $B^{[3]}$ -O and $B^{[4]}$ -O of 6P55 with (a) 5%, (b)10% and (c)15% B_2O_3/SiO_2 substitutions

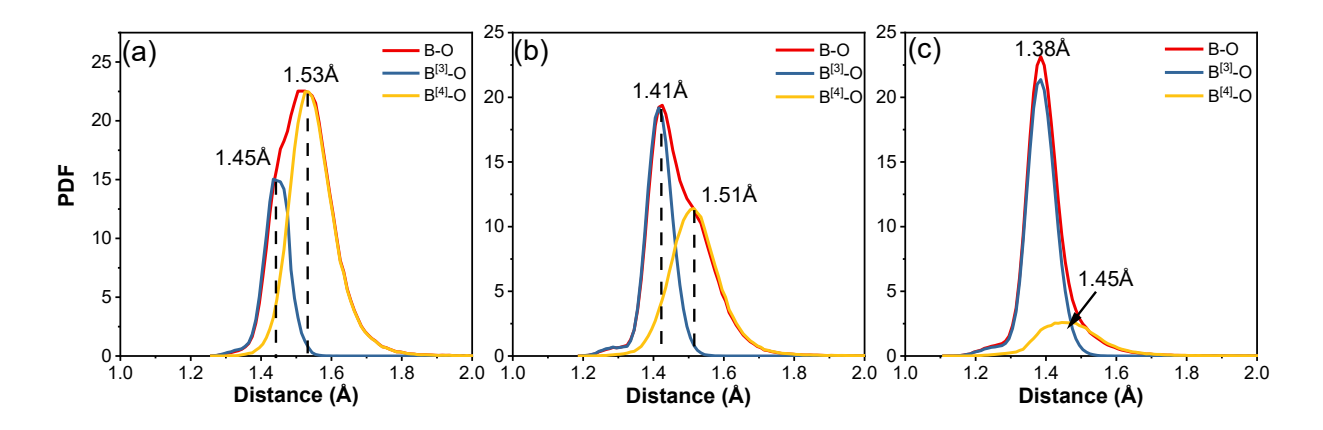


Figure 6 PDF of B-O and the deconvolution of $B^{[3]}$ -O and $B^{[4]}$ -O of 6P55 with (a) 5%, (b)10% and (c)15% BO_{3/2}/SiO₂substitutions

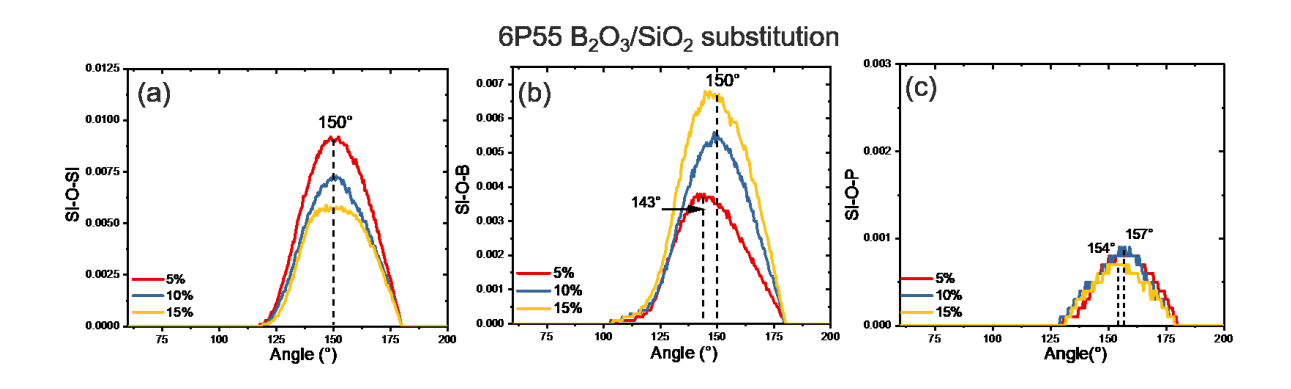


Figure 7 BAD of (a) ∠Si-O-Si, (b) ∠Si-O-B and (c) ∠Si-O-P of 1:2-gf-sub series

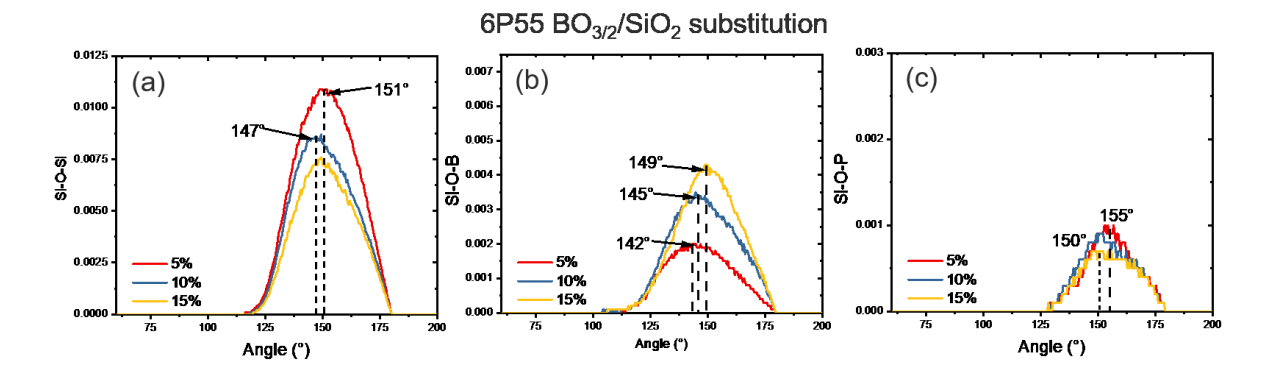


Figure 8 BAD of (a) ∠Si-O-Si, (b) ∠Si-O-B and (c) ∠Si-O-P of 1:1-gf-sub series

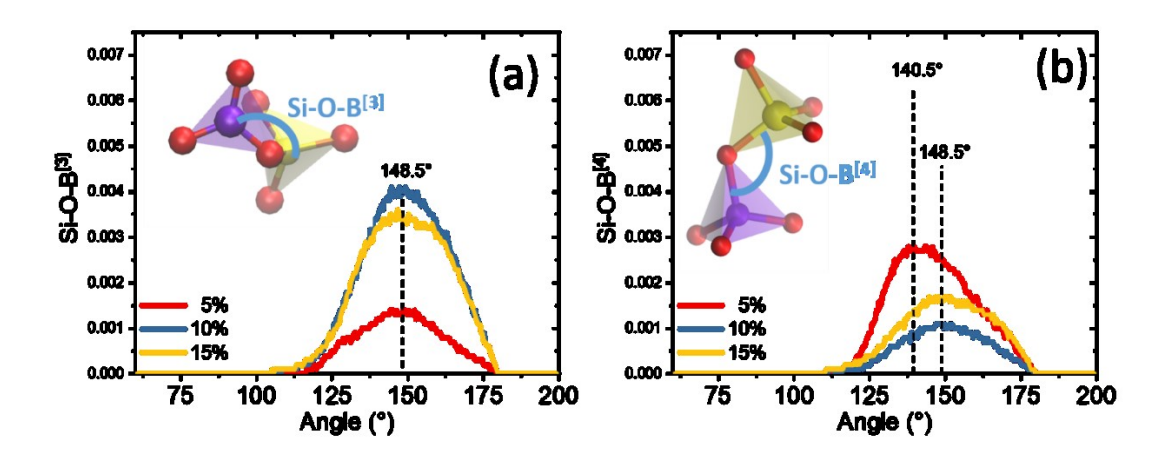


Figure 9 BAD of (a) \angle Si-O-B^[3] and (b) \angle Si-O-B^[4] in 1:2-gf-sub

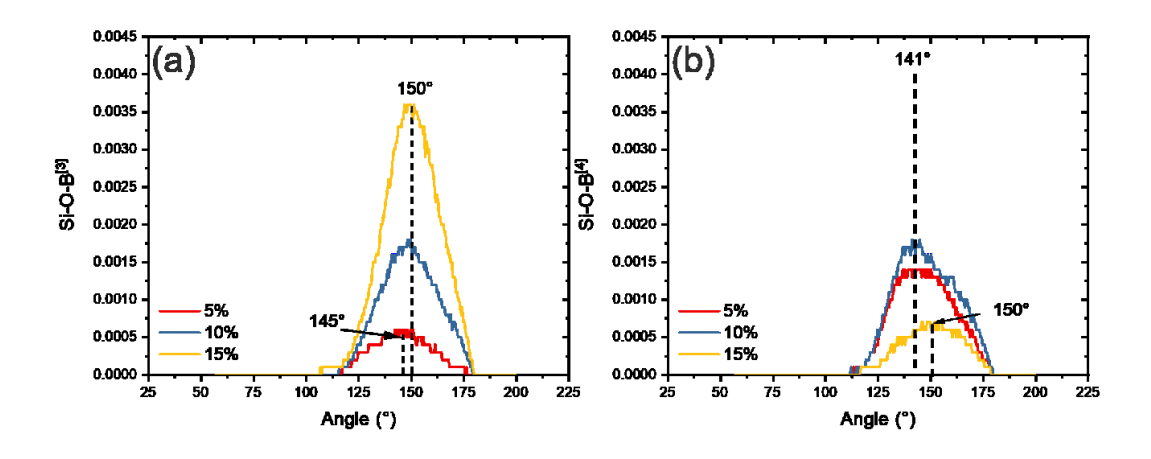


Figure 10 BAD of (a) $\angle Si\text{-O-B}^{[3]}$ and (b) $\angle Si\text{-O-B}^{[4]}$ in 1:1-gf-sub

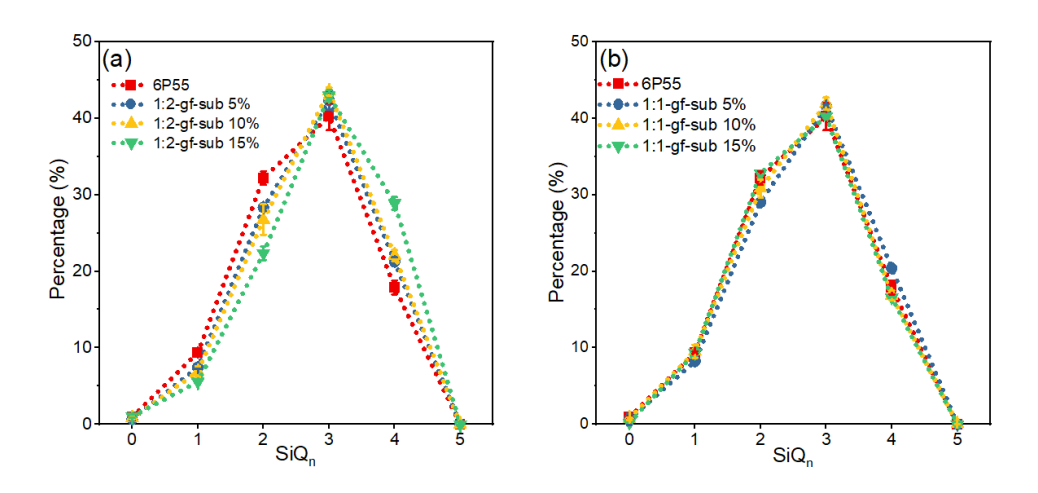


Figure 11 SiQn species distribution of (a) 1:2-gf-sub, (b) 1:1-gf-sub and 6P55

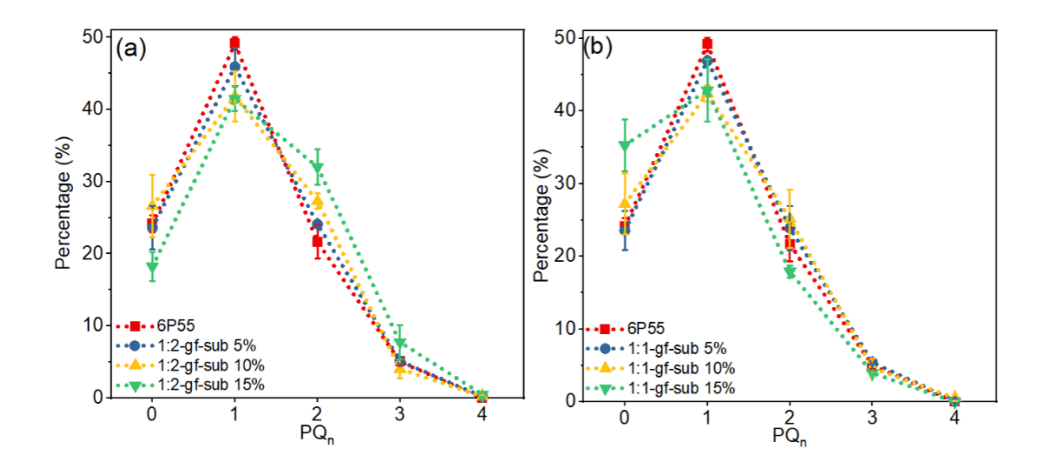


Figure 12 PQn species distribution of (a) 1:2-gf-sub and (b) 1:1-gf-sub vs 6P55

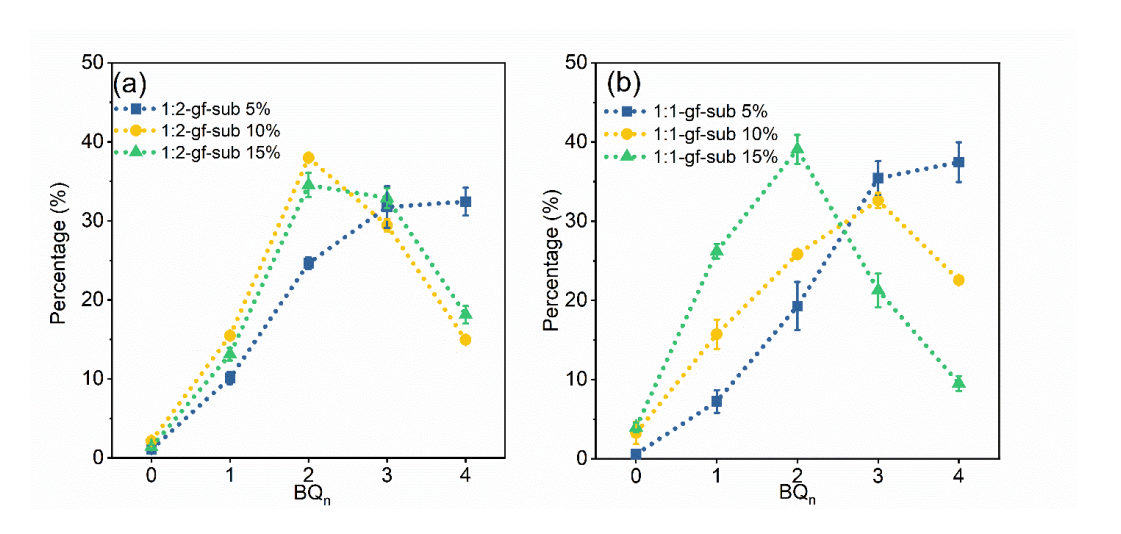


Figure 13 B_n species distribution of (a) 1:2-gf-sub and (b) 1:1-gf-sub

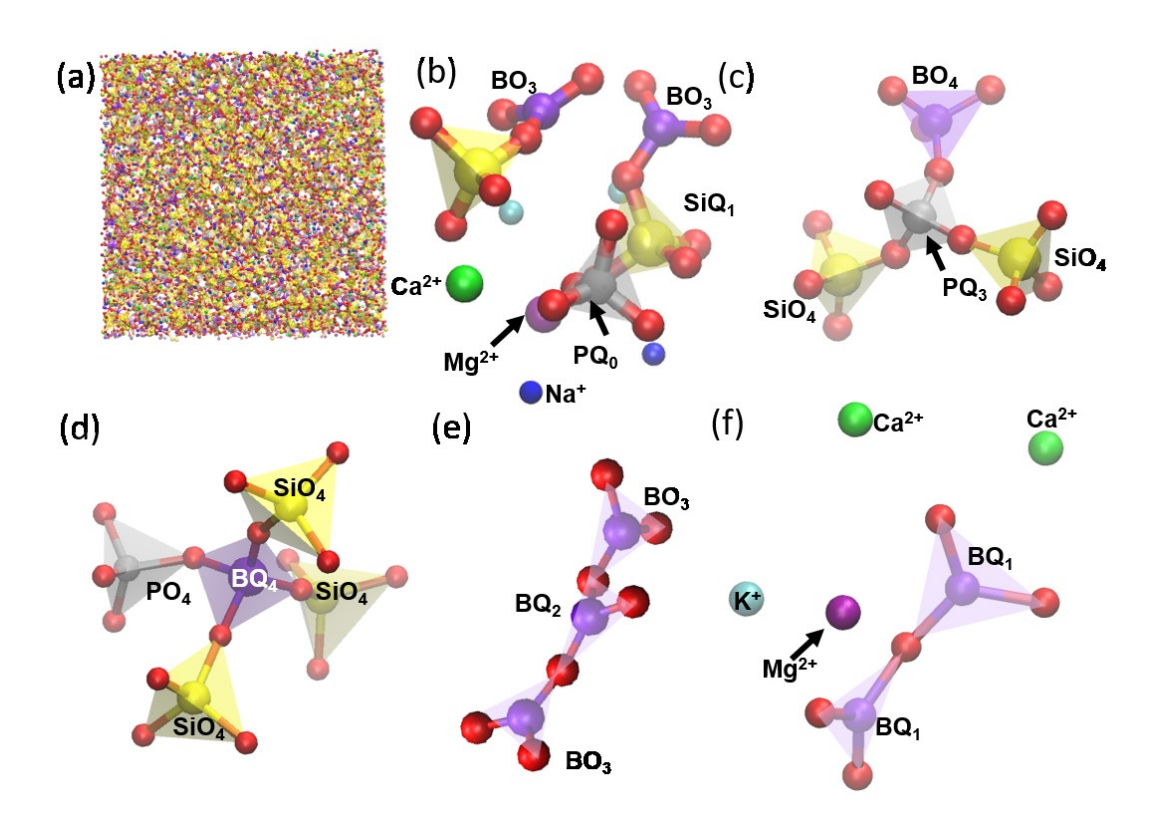


Figure 14 Snapshot of (a) 1:1-gf-sub 5% glass. Local structure of (b) PQ₀ from a single PO₄ with 4 NBOs, and (c) PQ₃ from a PO₄ corner-sharing with SiO₄ and BO₄ tetrahedrons. (d) BQ₄ from a BO₄ tetrahedron corner-sharing with PO₄ and SiO₄ tetrahedrons. (e) BQ₂ and (f) BQ₁ that composed by BO₃ units.

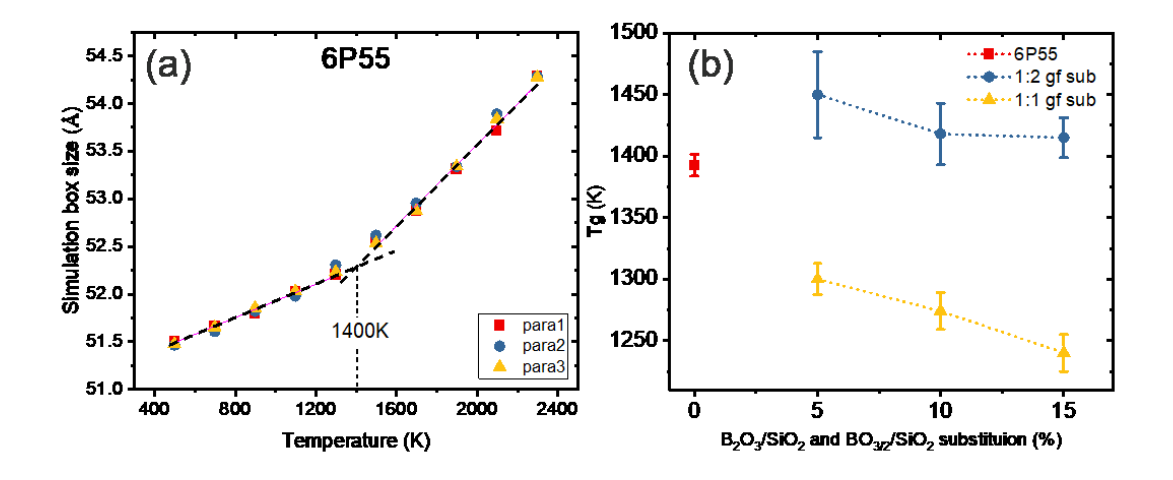


Figure 15 (a) T_g fitting of 6P55 and (b) T_g of 6P55, B₂O₃/SiO₂ and BO_{3/2}/SiO₂ substituted series

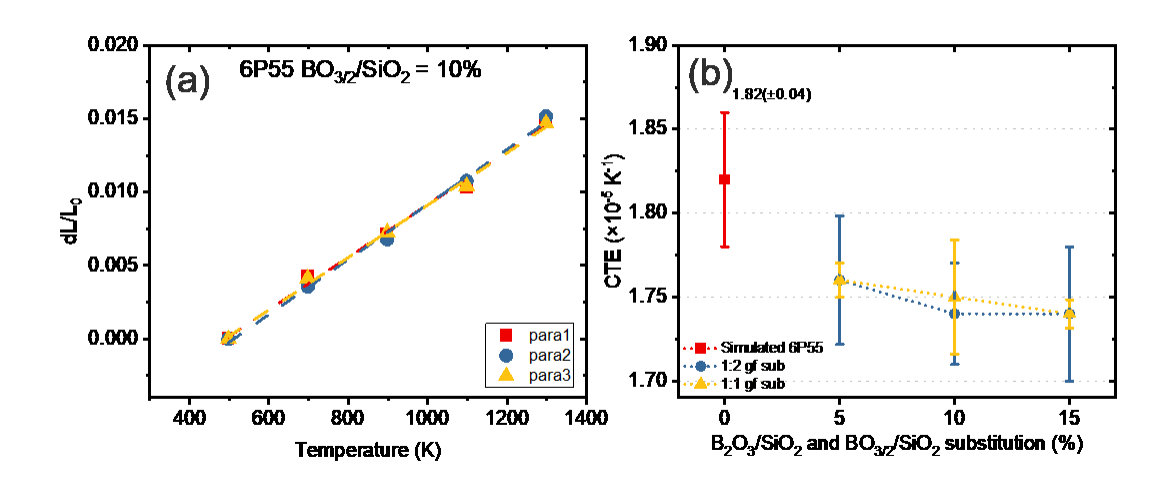


Figure 16 (a) CTE fitting for 6P55 with 10% $BO_{3/2}/SiO_2$ and (b) CTE of 6P55 and B_2O_3/SiO_2 and $BO_{3/2}/SiO_2$ substituted 6P55 series

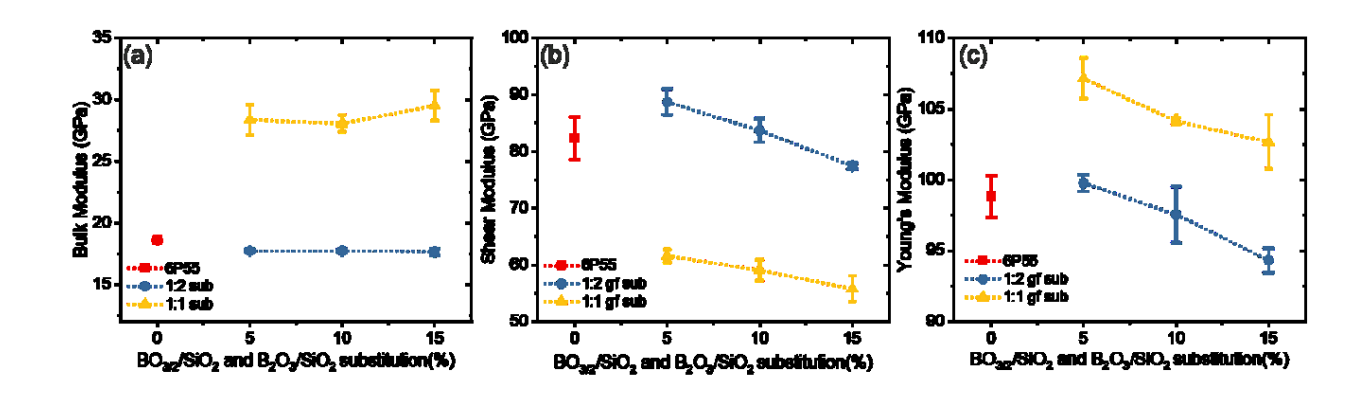


Figure 17 (a) Bulk modulus, (b) shear modulus and (c) Young's modulus of 6P55 and B_2O_3/SiO_2 and $BO_{3/2}/SiO_2$ substituted 6P55 series

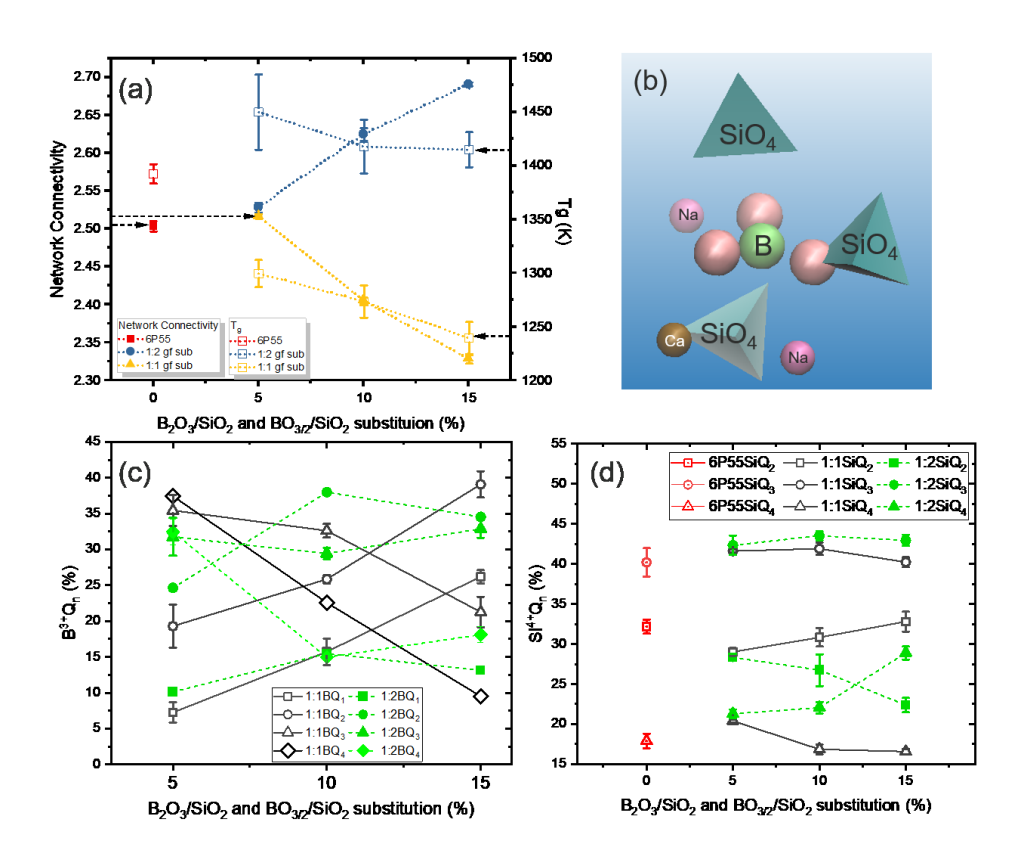


Figure 18 (a) Network connectivity (Solid) and T_g (hollow) (b) Snapshot of B₁^[3]in 15%BO_{3/2}/SiO₂ (c) B_n of 1:2-gf-sub (green) and 1:1-gf-sub (black) and (d) SiQ_n of 6P55 (red), 1:2-gf-sub (green) and 1:1-gf-sub (black)

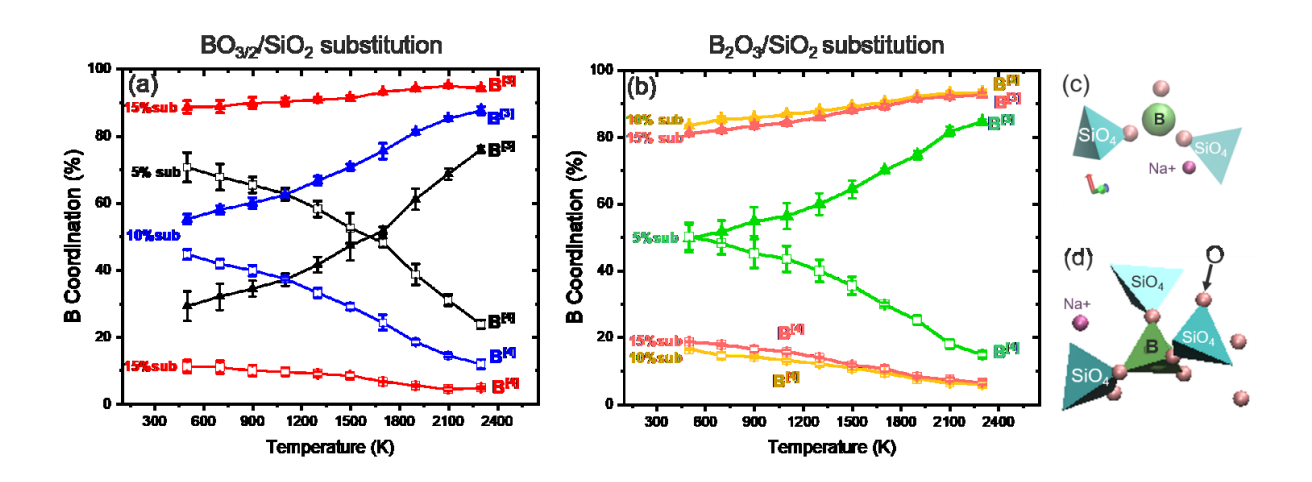


Figure 19 B^[3] and B^[4] of (a) 1:1-gf-sub series and (b) 1:2-gf-sub from 498K to 2298K. (c) Snapshot of $B_2^{[3]}$ and (d) $B_3^{[4]}$ from MD simulations

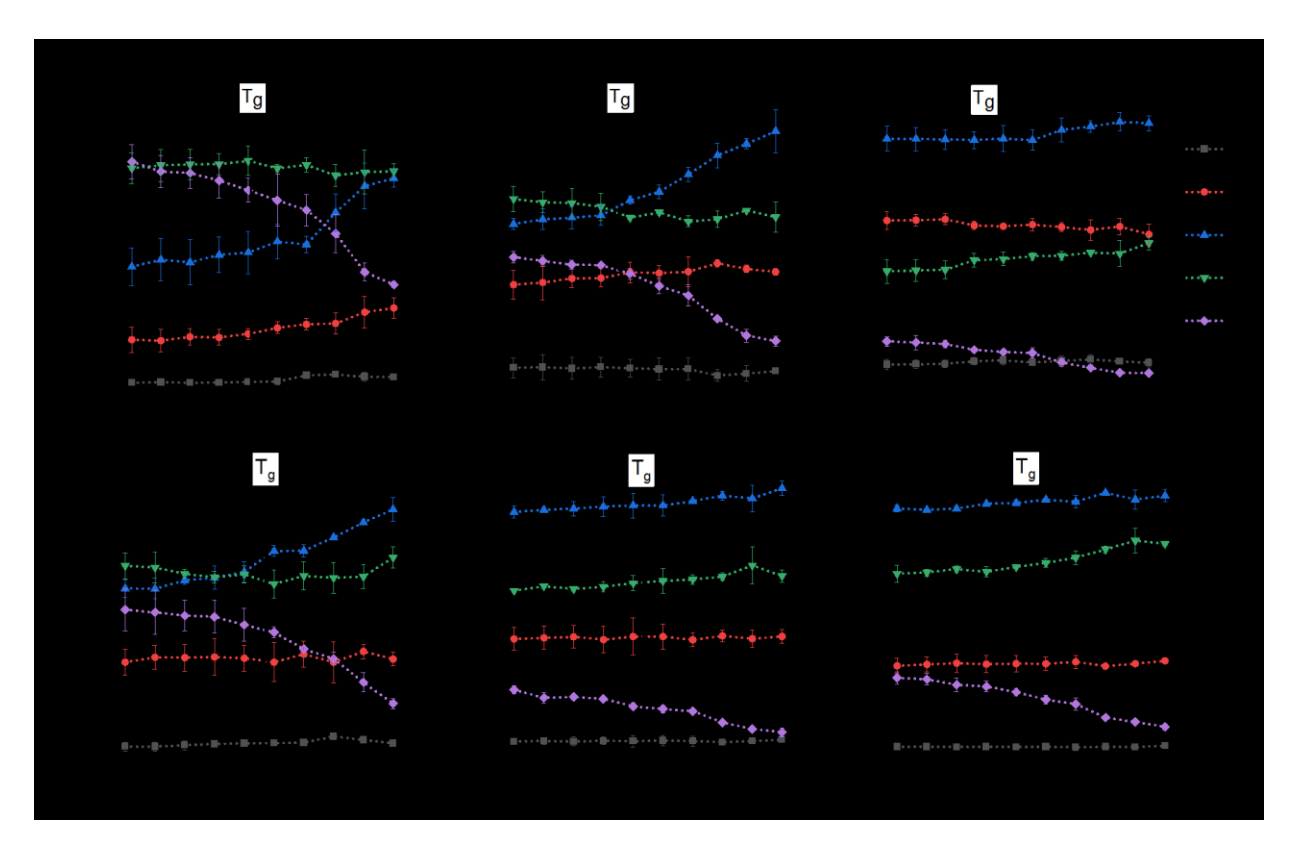


Figure 20 B_n species of (a) 5%, (b) 10% and (c) 15% of 1:1-gf-sub-series; and (d) 5%, (e) 10% and (f) 15% 1:2-gf-sub-series from 498K to 2298K

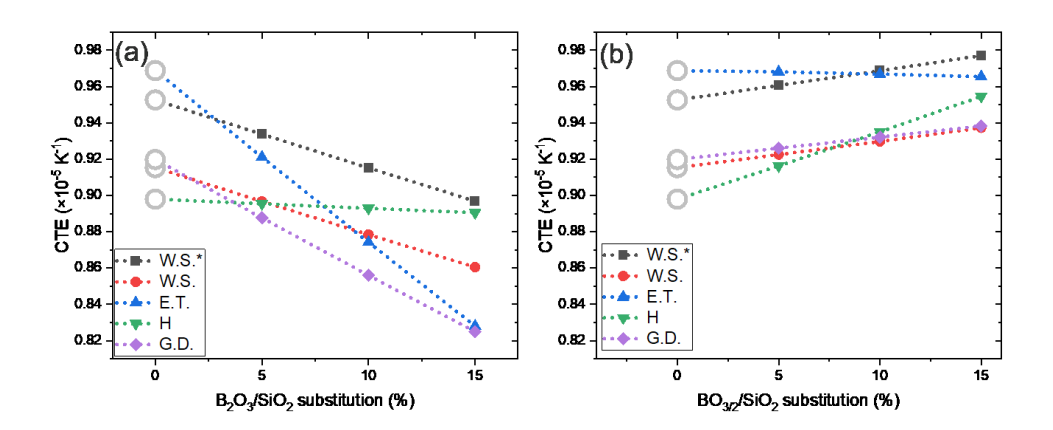


Figure 21 CTE of 6P55 and (a) 1:2-gf-sub and (b) 1:1-gf-sub derived from different models. The gray circle represents the CTE of 6P55 as the reference point

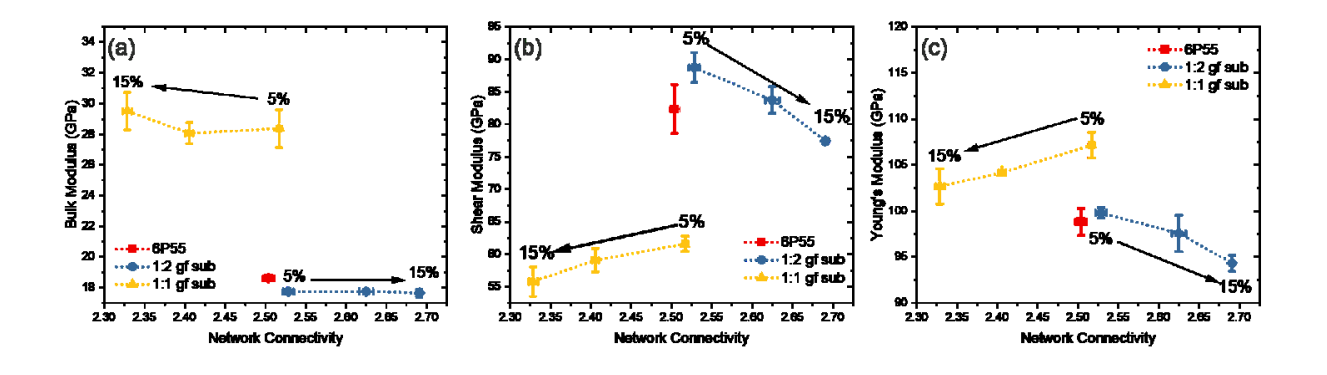


Figure 22 Network connectivity vs. (a) Bulk modulus (b) Shear modulus and (c) Young's Modulus of 1:2-gf-sub and 1:1-gf-sub glasses